



January 2016

Estimating Optically-Thin Cirrus Cloud Induced Cold Bias On Infrared Radiometric Satellite Sea Surface Temperature Retrieval In The Tropics

Jared Wayne Marquis

Follow this and additional works at: <https://commons.und.edu/theses>

Recommended Citation

Marquis, Jared Wayne, "Estimating Optically-Thin Cirrus Cloud Induced Cold Bias On Infrared Radiometric Satellite Sea Surface Temperature Retrieval In The Tropics" (2016). *Theses and Dissertations*. 2042.
<https://commons.und.edu/theses/2042>

This Thesis is brought to you for free and open access by the Theses, Dissertations, and Senior Projects at UND Scholarly Commons. It has been accepted for inclusion in Theses and Dissertations by an authorized administrator of UND Scholarly Commons. For more information, please contact zeinebyousif@library.und.edu.

ESTIMATING OPTICALLY-THIN CIRRUS CLOUD INDUCED
COLD BIAS ON INFRARED RADIOMETRIC SATELLITE SEA
SURFACE TEMPERATURE RETRIEVAL IN THE TROPICS

by

Jared Wayne Marquis
Bachelor of Science, University of Louisiana at Monroe, 2014

A Thesis

Submitted to the Graduate Faculty

of the

University of North Dakota

in partial fulfillment of the requirements

for the degree of

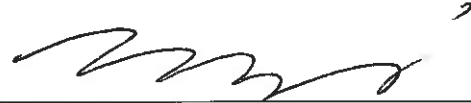
Master of Science

Grand Forks, North Dakota

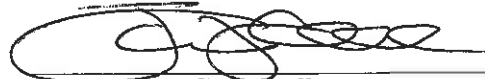
August

2016

This thesis, submitted by Jared Wayne Marquis in partial fulfillment of the requirements for the Degree of Master of Science from the University of North Dakota, has been read by the Faculty Advisory Committee under whom the work has been done and is hereby approved.



Dr. Jianglong Zhang



Dr. James Campbell



Dr. Matthew Gilmore

This thesis is being submitted by the appointed advisory committee as having met all of the requirements of the School of Graduate Studies at the University of North Dakota and is hereby approved.



Grant McGimpsey
Dean of the School of Graduate Studies

July 21, 2016

Date

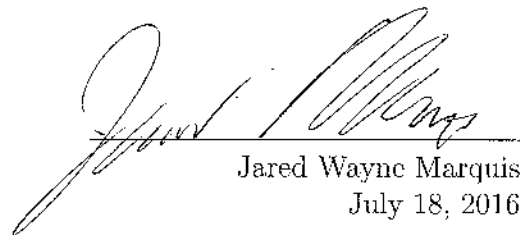
PERMISSION

Title Estimating Optically-Thin Cirrus Cloud Induced Cold
Bias on Infrared Radiometric Satellite Sea Surface Tem-
perature Retrieval in the Tropics

Department Atmospheric Sciences

Degree Master of Science

In presenting this thesis in partial fulfillment of the requirements for a graduate degree from the University of North Dakota, I agree that the library of this University shall make it freely available for inspection. I further agree that permission for extensive copying for scholarly purposes may be granted by the professor who supervised my thesis work or, in his absence, by the Chairperson of the department or the dean of the School of Graduate Studies. It is understood that any copying or publication or other use of this thesis or part thereof for financial gain shall not be allowed without my written permission. It is also understood that due recognition shall be given to me and to the University of North Dakota in any scholarly use which may be made of any material in my thesis.



Jared Wayne Marquis
July 18, 2016

TABLE OF CONTENTS

LIST OF FIGURES	v
LIST OF TABLES	vii
ACKNOWLEDGMENTS	viii
ABSTRACT	ix
CHAPTER	
I INTRODUCTION	1
Motivation	4
II DATASETS	9
Passive IR Satellite SST Products and Retrieval Models	9
CALIOP Cirrus Cloud Products	14
III METHODOLOGY	16
MODIS-CALIOP Collocation and Cloud Contamination	16
OTC SST Bias Estimates Using SBDART	17
Observational Representativeness	20
IV ANALYSIS	22
Collocation Statistics	22
Split-Window Bias Estimates	29
Triple-Window Bias Estimates	38
Verification	40
V CONCLUSIONS	42
APPENDICES	47
REFERENCES	49

LIST OF FIGURES

Figure		Page
1	The 5° x 5° occurrence frequency of a) cirrus and b) optically thin cirrus (OTC) over the tropics as retrieved from Cloud Aerosol Lidar with Orthogonal Polarization.	6
2	Numbers of collocated Level 2 Aqua-MODIS sea surface temperature (SST) and Level 2 CALIOP cloud-profiling pixels, for MODIS data Quality Levels (QL) 0 and 1, in 5° by 5° bins between 30° S and 30° N.	22
3	Relative frequencies of collocated Aqua-MODIS SST retrieval contamination, as identified by CALIOP, for a) all cloud, and b) all cirrus (defined as all clouds with a top height temperature -37°C).	23
4	Spatial extent of oceanic basins used in this study, with corresponding 5° by 5° bins depicted from 30° S and 30° N.	24
5	For collocated Aqua-MODIS SST and CALIOP cloud profile data pairs, the absolute difference between the raw QA product and that after cloud screening.	24
6	Relative frequencies of all residual cloud found in contaminated Level 2 Aqua-MODIS SST/CALIOP cloud profile data pairs as function of a) cloud top height and b) cloud top temperature, plotted globally and respectively for the Atlantic, Indian and Pacific Ocean basins (see insets).	25
7	Histograms of residual optically-thin cirrus (OTC) cloud optical depths for Aqua-MODIS SST QL 0 and 1 (see insets) for a) global, b) Atlantic Ocean basin, c) Indian Ocean basin, and d) Pacific Ocean basin.	28

8	SBDART radiative transfer model simulations of potential SST retrieval cold bias for an unscreened OTC as a function of cloud top height and optical depth for a) MODIS, b) AVHRR, and c) VIIRS. Overlaid on each composite are relative Aqua-MODIS/CALIOP collocated cirrus contamination occurrence frequencies (%).	29
9	As in Fig. 8, now for MODIS only over the a) Atlantic, b) Indian and c) Pacific Ocean basins.	35
10	SBDART radiative transfer model simulations of the ratio of the difference between the clear sky retrieved SST and the OTC-contaminated 11 and 12 μm brightness temperatures as a function of cloud top height and optical depth for a) MODIS, b) AVHRR, and c) VIIRS split-window algorithms.	37
11	SBDART radiative transfer model simulations of potential triple-window SST retrieval cold bias for an unscreened OTC as a function of cloud top height and optical depth for a) AVHRR, and b) VIIRS. Overlaid on each composite are relative Aqua-MODIS/CALIOP collocated cirrus contamination percentage occurrence frequencies (%).	38
12	Scatter plot of CALIOP cloud optical depth versus Aqua-MODIS SST from OTC-contaminated retrievals for August - October 2012 over the Maritime Continent (75°W/15°S 135°W/30°N).	40

LIST OF TABLES

Table		Page
1	Collocated data counts, all-cloud, all-cirrus, and optically-thin cirrus (OTC) contamination statistics calculated from Aqua-MODIS/CALIOP collocation globally and for the Atlantic, Indian and Pacific Ocean basins. Quality control refers to the MODIS Quality Level (QL) 0 and 1 Level 2 dataset used for collocation with CALIOP.	27
2	Mean absolute, or bulk mean, OTC cold biases in MODIS, AVHRR, and VIIRS SST split-window retrievals from SBDART simulations and assuming Aqua-MODIS/CALIOP collocated contamination frequencies, segregated as function of QL, global and Atlantic, Indian and Pacific Ocean basins. Absolute OTC cold biases for atmospheric profile with no water vapor and saturated column are given in parentheses, respectively.	32
3	As in Table 2, but for mean relative, or per contaminated observation, cold biases.	33
4	Mean absolute (relative) OTC cold biases in MODIS, AVHRR, and VIIRS SST triple-window retrievals from SBDART simulations and assuming Aqua-MODIS/CALIOP collocated contamination frequencies, segregated as function of QL, global and Atlantic, Indian and Pacific Ocean basins.	39
5	List of Abbreviations	48

ACKNOWLEDGMENTS

I would like to thank my advisor, Dr. Jianglong Zhang, and other committee members, Drs. James Campbell and Matthew Gilmore for their guidance and assistance through the course of this thesis work. I would also like to thank my collaborators, Alec Bogdanoff, Nathaniel Smith, and Drs. James Cummings and Douglas Westphal, for their research assistance. Brittany Carson receives a special thanks for her especially helpful editing. A special thanks is also required for my family, without whose love and support this wouldn't be possible. I would also like to thank my friends and fellow graduate students who provided relief and helped mold my graduate school experience.

ABSTRACT

Passive longwave infrared radiometric satellite-based retrievals of sea surface temperature (SST) at instrument nadir are investigated for cold bias caused by un-screened optically-thin cirrus (OTC) clouds (cloud optical depth ≤ 0.3 ; COD). Level 2 split-window SST retrievals over tropical oceans (30° S - 30° N) from Moderate Resolution Imaging Spectroradiometer (MODIS) radiances collected aboard the NASA Aqua satellite (Aqua-MODIS) are collocated with cloud profiles from the Cloud-Aerosol Lidar with Orthogonal Polarization (CALIOP) instrument, mounted on the independent NASA CALIPSO satellite. OTC are present in approximately 25% of tropical quality-assured (QA) Aqua-MODIS Level-2 data, representing over 99% of all contaminating cirrus found. This results in cold-biased SST retrievals using either split- (MODIS, AVHRR and VIIRS) or triple-window (AVHRR and VIIRS only) retrieval methods. SST retrievals are modeled based on operational algorithms using radiative transfer model simulations conducted with a hypothetical 1.5 km thick OTC cloud placed incrementally from 10.0 - 18.0 km above mean sea level for cloud optical depths (COD) between 0.0 - 0.3. Corresponding cold bias estimates for each sensor are estimated using relative Aqua-MODIS cloud contamination frequencies as a function of cloud top height and COD (assuming them consistent across each platform) integrated within each corresponding modeled cold bias matrix. Split-window relative OTC cold biases, for any single observation, range from 0.40° - 0.49° C for the three sensors, with an absolute (bulk mean) bias between 0.10° - 0.13° C. Triple-window retrievals are more resilient, ranging from 0.03° - 0.04° C relative and 0.11° - 0.16° C absolute. Cold biases are constant across the Pacific and Indian Ocean domains.

Absolute bias is smaller over the Atlantic, but relative bias is larger due to different cloud properties indicating that this issue persists globally.

CHAPTER I

INTRODUCTION

Sea surface temperature (SST) measurements are a core input for a host of meteorological and oceanographic modeling systems (e.g., Kelley et al. 2002; Harris and Maturi 2003; Tang et al. 2004; Donlon et al. 2007; Miyazawa et al. 2013). In theory, errors in background, or first guess, model SSTs can be mitigated by assimilating observed values, resulting in increased forecast skill. Tropical cyclone (TC) intensity forecasting, for instance, represents one specific area of significance for SST assimilation. Studies have shown exponential relationships between TC strength and SST using both maximum wind (DeMaria and Kaplan 1994) and minimum pressure (Miller 1958) as proxies for intensity. Thus, accurate SSTs are essential for accurate TC prediction. Additionally, El Niño-Southern Oscillation (ENSO) forecasts are highly dependent on SST values (Tang et al. 2004). The proper understanding and prediction of the global weather implications of ENSO require correct SST fields at model initialization.

While the spatial and temporal coverage of in-situ SST measurements are improving with the deployment of buoy networks (e.g., Roemmich et al. 2009), global daily measurements remain unavailable at resolutions finer than approximately 100 km. Thus, SSTs retrieved from passive radiometric remote sensors aboard earth-orbiting satellites are the primary source of fine resolution global estimates.

Retrievals of SST are based fundamentally on Planck's Law: the radiation emitted by an object is based upon that object's temperature and emissivity at the

emission wavelength. By measuring the amount of energy, or radiance, emitted by an object at a specific wavelength at an assumed known emissivity, the object's temperature can be retrieved through the equation:

$$T(\lambda, I_\lambda) = \epsilon \cdot \frac{hc}{k\lambda} \cdot \frac{1}{\log\left[\frac{2hc^2}{\lambda^5 I_\lambda} - 1\right]}, \quad (1.1)$$

where $T(\lambda, I_\lambda)$ is the retrieved temperature, ϵ is the object's emissivity, h is the Planck constant, c is the speed of light, k is the Boltzmann constant, and λ is the wavelength at which the radiance (I_λ) is measured. If ϵ is assumed to be 1, the resulting temperature is referred to as the brightness temperature. However, retrievals based upon this equation are only valid when the atmosphere between the object and the sensor measuring the radiance emitted by the object is transparent at the wavelength of measurement. A transparent atmosphere would not absorb or emit any radiation at a specific wavelength, and thus, all emitted radiance would be measured. In reality, the atmosphere is never transparent, and atmospheric correction is required.

Satellite measured radiance is a function of surface emitted and reflected radiance, the portion of that radiance that is extinguished by the atmosphere, atmospheric emitted and reflected radiance, and extinction of atmospheric radiance by the atmosphere. This relationship is given by the radiative transfer equation:

$$I_\lambda(\textit{measured}) = I_\lambda(\textit{surface})e^{-\tau(\textit{surface},\textit{satellite})} + \int_{\textit{surface}}^{\textit{satellite}} I_\lambda(\textit{layer})e^{-\tau(\textit{layer},\textit{satellite})}d(\textit{layer}), \quad (1.2)$$

where $I_\lambda(\textit{measured})$ is the satellite measured radiance, $I_\lambda(\textit{surface})$ is the upward radiance leaving the surface, $\tau(\textit{surface},\textit{satellite})$ is the optical depth between the surface and the satellite, $I_\lambda(\textit{layer})$ is the upward radiance leaving an atmospheric

layer, and $\tau(layer, satellite)$ is the optical depth between a layer and the satellite. Atmospheric correction attempts to solve for $I_\lambda(surface)$ using only the $I_\lambda(measured)$ term. If the atmosphere is transparent, $\tau(surface, satellite)$ and layer terms become zero, and $I_\lambda(measured)=I_\lambda(surface)$. In the case of SST retrieval, the atmospheric correction terms are solved through regression with in-situ observations. Importantly, the atmospheric correction is developed to account for only atmosphere as clouds are supposedly screened. Any unscreened cloud will cause the atmospheric correction to fail.

Satellite sensors launched in the 1960 - 1970s were only equipped with a short-wave infrared (IR) channel to retrieve SST because the atmosphere is nearly transparent at this wavelength (e.g., Deschamps and Phulpin 1980; Barton 1995). Atmospheric transparency is desired as it results in a higher signal to noise ratio, or more of the sensor retrieved signal being from the surface. However, shortwave channels are highly susceptible to errors associated with solar reflection during daylight hours, usually limiting the corresponding SST retrievals to nighttime only.

Beginning in 1979 with the launch of the NOAA-6 satellite, the Advanced Very High Resolution Radiometer (AVHRR) instrument afforded longwave IR channels at 10.8 and 11.9 μm wavelengths. This made daytime SST retrievals more practical though technique referred to as “split-window” because of the differences in water vapor absorption between the two channels (Llewellyn-Jones et al. 1984; McClain et al. 1985; Barton 1995; Davis 2007). While measurements at these longwave IR wavelengths are more sensitive to atmospheric water vapor, solar signal is negligible. The split-window technique is based upon the assumption that the difference between the true SST and brightness temperature near 11 μm is proportional to the difference between the true SST and brightness temperature near 12 μm due to their similar

atmospheric absorption characteristics (Merchant et al. 2009). This assumption is used to correct for atmospheric water vapor biases.

Triple-window algorithms for nighttime SST retrieval have also been developed that combine the 11 and 12 μm bands with the 3.9 μm shortwave band, thus using three channels for retrieval. Because water vapor absorption is significantly weaker at 3.9 μm than 11 or 12 μm , triple-window retrievals are considered more accurate. The addition of 3.9 μm measurements may also aid in cloud screening. Unfortunately, due to solar contribution in the 3.9 μm band, these measurements are currently limited to nighttime (Li et al. 2001). Uniquely, the Geostationary Operational Environmental Satellite (GOES) - 12 has used the 3.9 μm band for daytime retrievals using a split-window SST technique with the 11 μm band due to the instrument's lack of a 12 μm band. This retrieval is made possible by using radiative transfer model simulations to estimate and correct the solar contribution to the signal. As a result, processing time is increased and uncertainty in the solar contamination corrections result in lower overall fidelity (Merchant et al. 2009; Koner et al. 2015).

Satellite-borne passive infrared (IR) radiometers in current use for SST retrievals include: AVHRR (Walton 1988), GOES (Wu et al. 1999), the Moderate Resolution Imaging Spectroradiometer (MODIS; Brown and Minnett 1999), and the Visible Infrared Imaging Radiometer Suite (VIIRS; Petrenko et al. 2014). SST retrieval algorithms designed for each sensor are based on the specific IR channels available for each instrument.

Motivation

IR radiometers measure column-integrated radiances, and thus, the presence of typically colder-than-surface cloud and large aerosol particles will result in SST retrievals that are colder than in-situ. Retrievals are developed using the assump-

tion of clear skies. Consequently, existing SST algorithms are designed to identify and remove pixels containing cloud. Operational MODIS SST cloud screening, for instance, is achieved through a series of threshold, spatial homogeneity, and climatology tests (Brown and Minnett 1999). Despite efforts by other passive IR radiometer algorithms to correct for cloud, contamination still remains—particularly with respect to optically-thin cirrus (OTC) clouds. Sassen and Cho (1992) define these unique clouds as exhibiting translucence with respect to blue sky above them, as evident to a ground observer. Conversely, a nadir-viewing passive IR radiometric imager is presumably dominated by the relatively warm ground below, making these clouds difficult to distinguish relative to surrounding clear skies or background surface features in terms of spatial and thermal contrast.

Holz et al. (2008) demonstrated how the lower threshold sensitivity of the MODIS cloud product tends to occur very near a cloud optical depth (COD) of 0.30, approximately upper threshold of OTC presence advocated by Sassen and Cho (1992). Similar bias has been identified in the MODIS aerosol product. Toth et al. (2013) reported the presence of both cirrus and low-topped, near-surface clouds in otherwise quality-assured MODIS aerosol optical depth retrievals. Huang et al. (2013) also found the presence of cirrus causing contamination in MODIS aerosol retrievals. Ground-based solar/near-IR radiometers used by the Aerosol Robotic Network (AERONET) have been found to exhibit significant OTC contamination (Chew et al. 2011; Huang et al. 2011). Although various satellite retrieved SST products implement different cloud clearing algorithms, evidence within the cited literature strongly suggests that passive IR radiometric algorithms exhibit limited skill in detecting OTC due to sensor limitations.

Unlike passive radiometers that measure emitted or reflected solar energy, active sensors emit a pulse of energy and measure the reflection of this energy off

of objects. Ergo, an active sensor can easily measure thin clouds. Specifically, light detection and ranging (LiDAR) sensors can observe OTC. The Cloud Aerosol LiDAR with Orthogonal Polarization (CALIOP; Winker et al. 2010) aboard the Cloud-Aerosol Lidar and Infrared Pathfinder Satellite Observation (CALIPSO; Stephens et al. 2002; Winker et al., 2009, 2010) satellite can be used to determine cloud contamination in retrieved products from the MODIS sensor aboard the Aqua satellite (e.g., Toth et al. 2013). Both CALIPSO and Aqua fly in the satellite constellation referred to as the A-Train, and thus, virtually observe the scene at the same time.

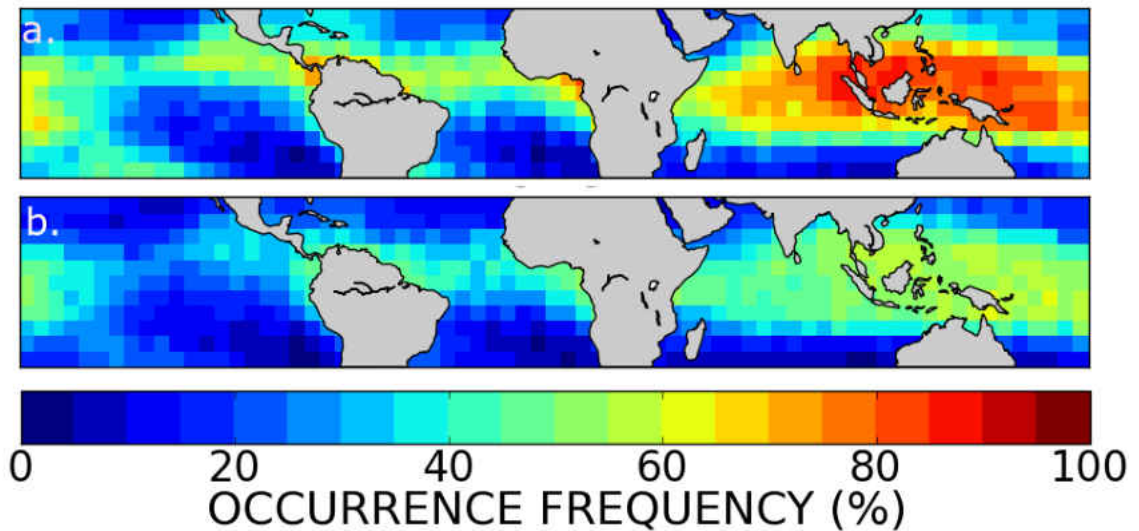


Figure 1: The $5^\circ \times 5^\circ$ occurrence frequency of a) cirrus and b) optically thin cirrus (OTC) over the tropics as retrieved from Cloud Aerosol Lidar with Orthogonal Polarization.

Residual cirrus clouds present a significant concern for IR SST retrievals due to their high effective altitude, cold cloud tops, and elevated relative occurrence. CALIOP-observed (a) cirrus and (b) OTC frequency of occurrence in the tropics are shown in Figure 1. Cirrus is present in approximately 50-90% of all equatorial scenes, corresponding with the inter-tropical convergence zone. Specifically, over the Maritime Continent of Southeast Asia, cirrus is present in 70-90% of all scenes. Cirrus

occurrence decreases with increasing latitude, to a minimum of roughly 10% at $\pm 30^\circ$ latitude. Compared to cirrus, OTC occurrence is similar in distribution, though less frequent. Maximum OTC occurrence, again, occurs over the Maritime Continent at a rate of approximately 40-60%. Equatorial regions exhibit OTC occurrence rates of nearly 40%, dropping to roughly 10% with increasing latitude. Given the extremely high occurrence and cold cloud tops, both cirrus and OTC have greater potential for significant radiance contamination and aliasing at IR wavelengths than atmospheric aerosols.

To date, the cold biasing of IR satellite-retrieved SSTs has only been discussed quantitatively for unscreened dust and volcanic aerosols (e.g., Merchant et al. 1999; Bogdanoff et al. 2015) and only qualitatively for cloud contamination (e.g., Merchant and Le Borgne 2004; Vázquez-Cuervo and Armstrong 2004; Hosoda 2011; Merchant et al. 2012). Similar to OTC, aerosols act as strong longwave absorption and emission sources that contaminate sea surface emission signals and SST retrievals. Nevertheless, significant aerosol plumes, such as dense dust storms, occur less frequently and over limited spatial and temporal domains compared to cirrus. However, aerosol plumes are most prominent at significantly lower altitudes and warmer temperatures than cirrus, which result in less thermal contrast with the sea surface and a relatively weaker associated SST cold bias overall.

As mentioned, NASA's A-Train presents a unique opportunity for the pairing passive IR radiometric and active-based remote sensing instruments, using Aqua and CALIPSO satellites, for investigating the cold biasing of IR SST retrievals by OTC. This paper describes a series of such experiments using paired MODIS/CALIOP measurements to, first, identify residual OTC contamination properties within the MODIS SST retrieval product and, then, estimate corresponding SST cold biases for split-window and triple-window IR algorithms developed for MODIS, VIIRS and AVHRR.

Using techniques similar to Bogdanoff et al. (2015) for aerosols, a one-dimensional radiative transfer model is used to simulate SST retrieval algorithm performance by modeling OTC contamination for the different sensors, methodologies, and corresponding channels. CALIOP/MODIS cloud contamination properties are assumed consistent across VIIRS and AVHRR for the modeling experiments. The goal of this work is a broad-scale assessment of the impact of OTC on operational IR radiometric satellite oceanographic sensors.

CHAPTER II

DATASETS

Passive IR Satellite SST Products and Retrieval Models

Examination of cloud contamination bias is performed for the MODIS, AVHRR, and VIIRS sensors. Specifically, the MODIS sensor aboard the Aqua satellite, the AVHRR sensor aboard MetOp-A, and the VIIRS sensor aboard the Suomi-NPP satellite are used. Aqua is positioned in a sun-synchronous orbit in the satellite constellation known as the A-Train, crossing the equator at approximately 1:30 (both AM and PM) local solar time. MetOp-A and Suomi-NPP are also sun-synchronous crossing the equator at approximately 9:30 AM and 1:30 AM and PM, respectively. While both Aqua and Suomi-NPP cross the equator at similar local solar times, Aqua crosses the equator in daylight while Suomi-NPP crosses the equator at night. Thus, Aqua and Suomi-NPP are approximately at opposite ends of the globe at any given time. To create high confidence cloud contamination results, only the MODIS retrieved SST product is collocated with CALIOP cloud retrievals. Because CALIOP (aboard CALIPSO) also flies in the A-Train, observations of from each sensor will be collected within 5 minutes of each other. The methodology used for this collocation is explained in the following chapter.

Daily 1-km 11 and 12 μm split-window retrieved SST values from the Level 2 Aqua-MODIS SST product (MOD28; available online¹) from January through December of 2012 are used to collocate with CALIOP. To the author's knowledge, at

¹<http://oceandata.sci.gsfc.nasa.gov/MODISA/L2/>

the time of this publication, there is not an operational MODIS triple-window retrieval. Each MODIS SST retrieval is assigned a quality level (QL) between 0 and 4 (0 indicating no quality flags or a perfect retrieval; 4 indicating a failed retrieval). QL is determined through a series of tests. Specifically, these tests include spatial homogeneity tests (i.e., pixel-by-pixel “buddy checks”), climatology-deviation tests to remove unrealistic values, and baseline-deviation checks that look to filter values that represent a clear deviation from the weekly Optimum Interpolation Sea Surface Temperature (OISST; Reynolds and Smith 1994; Brown and Minnett 1999). The author is not aware of defined operational protocols for working with the MODIS SST product. In this study, it is assumed that QL of 0 and 1 are of sufficient fidelity so as to be referred to as quality assured (QA) data. In contrast, $QL > 1$ are considered to represent retrievals with significant ($>3^\circ$ C) deviations from climatology or baseline values that are sufficiently indicative of contamination (possibly cloud). A summary of the MODIS SST product, QL flags, and tests is available online ². Results described below are shown for each of $QL=0$, $QL=1$, and QA for completeness.

Split-window MODIS IR SST retrievals are conducted using measured radiances at the 11.03 and 12.02 μm bands, chosen as they exhibit significant differences in water vapor absorption and proximity to the average planetary blackbody emission temperature (Brown and Minnett 1999). Retrievals are performed through the following system of equations (Brown and Minnett 1999):

for $\Delta T_B \leq 0.5$:

$$SST = a_{00} + (a_{01} \cdot T_{B_{11}}) + (a_{02} \cdot \Delta T_B \cdot \overline{SST}) + (a_{03} \cdot \Delta T_B \cdot (\frac{1.0}{\mu} - 1)), \quad (2.1)$$

²<http://oceancolor.gsfc.nasa.gov/cms/atbd/sst/>

for $\Delta T_B \geq 0.9$:

$$SST = a_{10} + (a_{11} \cdot T_{B_{11}}) + (a_{12} \cdot \Delta T_B \cdot \overline{SST}) + (a_{13} \cdot \Delta T_B \cdot (\frac{1.0}{\mu} - 1)). \quad (2.2)$$

Here, ΔT_B is the difference between the brightness temperature at the 11 μm and 12 μm bands, $T_{B_{11}}$ is the brightness temperature at the 11 μm band, \overline{SST} is a baseline SST value created by bilinear interpolation of the OISST product or a near-IR retrieved SST value (from the previous night's retrieval), μ is the cosine of the sensor zenith angle, and each a coefficient is continuously tuned and optimized through verification with in-situ buoy observations. For values of ΔT_B greater than 0.5 and less than 0.9, the retrieved SST is equal to the linear interpolation of the above equations with respect to ΔT_B . Uncertainties arise in the deriving of operational coefficients due to ambiguities in relating buoy observations with satellite radiances and the possible presence of OTC. For simulations of this retrieval described in Chapter III, the a coefficients used are: $a_{00}=1.1010$; $a_{01}=0.9470$; $a_{02}=0.1710$; $a_{03}=1.4210$; $a_{10}=1.8820$; $a_{11}=0.9350$; $a_{12}=0.1230$; $a_{13}=1.3720$.

The MetOp-A AVHRR split-window SST retrieval is performed using radiances at the 10.8 and 11.9 μm bands, from Channels 4 and 5, using the following equation from the Naval Oceanographic Office (NAVO) Nonlinear SST (NLSST) algorithm (Walton et al. 1998):

$$SST = a_0 + (a_1 \cdot T_{B_4}) + (a_2 \cdot \Delta T_B \cdot \overline{SST}) + (a_3 \cdot \Delta T_B \cdot (\frac{1.0}{\mu} - 1)), \quad (2.3)$$

where T_{B_4} is the brightness temperature from Channel 4, ΔT_B is the difference in brightness temperatures between Channels 4 and 5, \overline{SST} is a baseline or climatological SST, μ is the cosine of the sensor zenith angle, and the coefficients, a_1 , a_2 , and a_3 , are tuning constants again based on optimization between retrievals and observations

from global drifting buoys. Note the similarity of this relation with the equations used in the MODIS retrieval. To model this retrieval, a set of operational coefficients provided by NAVO and used by Bogdanoff et al. are applied (2015; $a_0=-263.3489$; $a_1=0.9690$; $a_2=0.0772$; $a_3=1.0318$).

The NPP-Suomi VIIRS split-window retrieval algorithm applies radiances at the 10.80 and 12.05 μm bands from Channels 15 and 16 to retrieve SST (Brisson et al. 2002; Merchant et al. 2008; Petrenko et al. 2014), using the following equation:

$$SST = a_0 + (a_1 \cdot T_{B_{15}}) + (a_2 \cdot T_{B_{15}} \cdot \frac{1.0}{\mu}) + (a_3 \cdot \Delta T_B) + (a_4 \cdot \Delta T_B \cdot \overline{SST}) + (a_5 \cdot \Delta T_B \cdot \frac{1.0}{\mu}) + (a_6 \cdot \frac{1.0}{\mu}), \quad (2.4)$$

where $T_{B_{15}}$ is the brightness temperature from Channel 15, ΔT_B is the difference in brightness temperatures between Channels 15 and 16, μ is the cosine of the sensor zenith angle, \overline{SST} is the Level 4 SST provided from the Canadian Met Center (or other Level 4 SST product if unavailable), and the coefficients, a_0 through a_6 , are again the optimized tuning constants. The set of coefficients used to model the retrieval here come from the Advanced Clear-Sky Processor for Oceans (ACSPO) SST algorithm as of July 2015 (Boris Petrenko, *personal communication* 2015; $a_0=5.623045$; $a_1=0.985192$; $a_2=0.019775$; $a_3=0.456758$; $a_4=0.067732$; $a_5=0.705117$; $a_6=-4.714369$).

Algorithms using triple-window retrieval techniques are also available for AVHRR and VIIRS. The MetOp-A AVHRR triple-window SST is retrieved using:

$$SST = a_0 + (a_1 + [a_2 \cdot (\frac{1.0}{\mu} - 1)]) \cdot T_{B_{3.7}} + (a_3 + [a_4 \cdot (\frac{1.0}{\mu} - 1)]) \cdot \Delta T_B + [a_5 \cdot (\frac{1.0}{\mu} - 1)], \quad (2.5)$$

where $T_{B_{3.7}}$ is the brightness temperature from the 3.7 μm band, ΔT_B is the difference in brightness temperatures between Channels 4 and 5, μ is the cosine of the sensor zenith angle, and the coefficients, a_{0-5} are tuning constants. For modelling the retrieval below, the set of coefficients applied are described by Météo-France ($a_0=1.15351$; $a_1=0.02109$; $a_2=0.02109$; $a_3=0.68858$; $a_4=0.33056$; $a_5=1.27303$; Le Borgne et al. 2007).

The operational NAVO NPP-Suomi VIIRS triple-window algorithm features the equation:

$$SST = a_0 + (a_1 \cdot T_{B_{3.7}}) + (a_2 \cdot \overline{SST} \cdot \Delta T_B) + [a_3 \cdot (\frac{1.0}{\mu} - 1)] + (a_4 \cdot \Delta T_B) + [a_5 \cdot (\frac{1.0}{\mu} - 1)] + [a_6 \cdot \overline{SST} \cdot (\frac{1.0}{\mu} - 1) \cdot \Delta T_B], \quad (2.6)$$

where $T_{B_{3.7}}$ is the brightness temperature from the 3.7 μm band, ΔT_B is the difference in brightness temperatures between Channels 15 and 16, μ is the cosine of the sensor zenith angle, \overline{SST} is a baseline SST, and the coefficients, a_{0-6} , are tuning constants. Here, the operational coefficients used in this study are provided by NAVO ($a_0=-276.0353$; $a_1=1.0139$; $a_2=0.0027$; $a_3=1.4069$; $a_4=0.8880$; $a_5=-0.4000$; $a_6=0.0269$).

3em Quality-testing and cloud clearing for the retrieval algorithms of each sensor vary slightly and stem from the tests created for the AVHRR Pathfinder algorithm described in Kilpatrick et al. (2001). Specifically, the MODIS cloud clearing and quality control algorithm is based upon the use of brightness temperature difference thresholds and spatial homogeneity from IR measurements within the atmospheric window region. If a pixel passes the previous tests, the retrieved SST is, then, required to be within a specific range of the expected SST (from climatology or previous retrieval; Brown and Minnett 1999). The VIIRS cloud algorithm is identical to the MODIS algorithm based upon the Miami Decision Tree (Minnett et al. 2013).

In contrast to the MODIS and VIIRS retrieval algorithms, the MetOp-A AVHRR retrieval algorithm references both IR and visible channels for cloud clearing through threshold and spatial homogeneity tests (Levanant et al. 2007).

Whereas collocation is possible only between CALIOP and MODIS due to temporal constraints, VIIRS and AVHRR cloud clearing efficiency cannot be independently characterized using the aforementioned methodology. Modeling of OTC bias in those datasets, described in Chapters III and IV, requires some knowledge of contaminating OTC properties. Thus, as introduced above, this study assumes that OTC contamination is consistent across the three radiometers. Contamination properties relating cloud top heights and relative frequencies from MODIS/CALIOP are, thus, extrapolated to VIIRS and AVHRR.

CALIOP Cirrus Cloud Products

CALIOP cirrus cloud observations considered in this study come from the Version 3.02 Level 2 CALIPSO 5-km cloud layer product (available online³). This product includes cloud top and base heights, corresponding temperatures, and cloud optical depths (COD). Cloud temperatures come from Goddard Model Assimilation Office (GMAO) Goddard Earth Observing Model-Version 5 data embedded within the product. This product was chosen for its integration of resolved cloud layers at multiple spatial resolutions (5, 20, and 80 km; Vaughan et al. 2009), which more readily include OTC. Clouds resolved with CALIOP algorithms at finer resolution (0.33 and 1.00 km) are not included in this product as they likely represent spatially-inhomogeneous liquid water clouds and not cirrus.

Cirrus clouds are specifically distinguished in the CALIOP dataset by applying a maximum cloud top temperature of -37° C. The basis for applying this thermal

³<https://eosweb.larc.nasa.gov/>

threshold is motivated by Campbell et al. (2015). Though conservative, significant ambiguity arises from interpreting autonomous LiDAR signals, and distinguishing warm cirrus (typically, sheared fallstreaks decoupled from their parent cloud that give the appearance of a cirrus cloud with an apparent top height temperature warmer than -37°C) from glaciated liquid water clouds that are mixed phase, and thus, not cirrus in the phenomenological sense. These latter clouds feature ice microphysical characteristics that are sufficiently different than traditional cirrus. Thereby, to constrain the radiative transfer simulations described in the next chapter, only clouds with tops colder than -37°C are considered as cirrus.

COD is used as the dependent variable for estimating SST retrieval cold biases. COD uncertainties in the CALIPSO 5-km cloud layer product used have recently been characterized by Garnier et al. (2015). CALIOP COD algorithms perform either constrained retrievals, where COD is solved directly by comparing molecular atmospheric backscatter returns above and below the cloud, or unconstrained ones, where molecular returns below the cloud cannot be estimated and an a-priori relationship between cloud extinction and backscatter coefficients is applied based on cloud centroid temperature to solve COD (Vaughan et al. 2009; Young and Vaughan 2009). Whereas we are dealing almost exclusively with relatively low COD cases with OTC, our sample compositions tend strongly toward constrained retrievals for which we anticipate low relative error.

CHAPTER III

METHODOLOGY

MODIS-CALIOP Collocation and Cloud Contamination

Collocation was performed for the year of 2012 over tropical oceans (30° S - 30° N). The tropical latitudes are investigated given the significant occurrence frequencies for cirrus found there, causing presumably greater cold biasing of SST, relative to global conditions (Mace et al. 2009). The tropics are also particularly interesting due to the importance of accurate SST retrievals in this region. Namely, this region is important to both ENSO and tropical cyclone forecasting. However, as will be discussed in Chapter IV, assumptions about regions outside of the tropics can be made given the results here.

MODIS retrieves SST at 1 km^2 spatial resolution. Collocation between Aqua-MODIS and the 5 km by 70 m CALIOP product was performed by identifying those QA MODIS SST 1 km^2 pixel centers within 1 km of the CALIOP LiDAR ground track. Specifically, the ground track was found through linear interpolation of the 5 km CALIOP product center location. Once the linear ground track was found, distance from the linear ground track to the center of each MODIS retrieved SST pixel is determined. Pixel centers within 1 km of the linear ground track were, then, collocated with the nearest 5 km CALIOP center pixel. Frequency of contamination is reported by cloud type (all cirrus, OTC, and other) and QA level. Residual cloud top altitudes, temperatures, and COD are also examined. Contamination statistics are described in Chapter IV.

This collocation technique could result in a CALIOP cloud layer pixel being collocated with a maximum of 14 MODIS retrieved SST pixels. However, because of the spatial characteristics of the product only containing cloud information resolved at 5 km, this should not induce a high bias in residual cirrus frequency. Conversely, estimates of residual stratocumulus are expected to be low as these clouds are unlikely resolved at 5 km. Because this study only focuses on cirrus due to the extreme difference in SST and cirrus cloud top temperature, in certain areas globally, stratocumulus may be the dominate species of cloud. Thus, future examination into stratocumulus bias should be completed.

OTC SST Bias Estimates Using SBDART

OTC cold bias estimates for each of the satellite retrievals were solved through radiative transfer simulations using the Santa Barbara DISORT Atmospheric Radiative Transfer model (SBDART; Ricchiazzi et al. 1998). Following the methodology used by Bogdanoff et al. (2015), top-of-atmosphere radiance values for sensor nadir were calculated using SBDART as equipped with a standard tropical atmosphere and surface temperature of 26.85° C that is assumed the corresponding profile SST. A two-dimensional SST cold bias array of solutions for MODIS, VIIRS and AVHRR split-window and VIIRS and AVHRR triple-window retrievals is created by simulating a 1.5 km thick OTC layer present at varying top height altitudes (10.00 - 18.00 km in 0.25 km segments, all heights above mean sea level; MSL) and COD (0.00 - 0.30, in 0.01 segments from 0.01-0.06 and 0.02 segments above 0.06).

Mean OTC SST bias values were estimated by integrating the product of the frequency of OTC-only occurrence for each altitude/COD bin and the corresponding SST cold bias modeled with SBDART. Only single layer OTC is considered in these frequencies. Residual multiple layer OTC, cirrus, non-cirrus cloud, or combination of

would likely cause more bias as the column integrated COD is larger. Due to ambiguity in cloud positions, bias for these multiple layered clouds is not solved. Relative bias, defined as the mean bias of all OTC-only contaminated retrievals, was calculated using only the relative frequency of occurrence. Finally, the absolute bias is the mean bias of all pixels assuming only OTC contamination (i.e., relative bias normalized by the frequency of OTC occurrence) given by the absolute frequency of occurrence. As a subsequent sensitivity test, the proportionality between the difference in the SST and brightness temperatures from 11 μm and 12 μm channels is examined for each sensor, given that the split-window technique is based upon the assumption that this relationship is constant.

The core SBDART module simulates cirrus clouds as spherical ice grains (Ricchiuzzi et al. 1998). Yang et al. (2005), however, reported that differing ice particle structures result in significant variance in absorption efficiency at the wavelengths used in the SST retrievals. Thus, a modified version of the SBDART ice microphysical scheme consistent with that of the ice particle structures defined in Yang et al. (2005) was developed. For particles with effective radius smaller than 35 μm , the augmented ice microphysical scheme assumes 50% bullet rosettes, 25% hollow columns, and 25% plates. For particles with effective radius larger than 35 μm , the scheme assumes 30% aggregates, 30% bullet rosettes, 20% hollow columns, and 20% plates (Yang et al. 2005). Within cloud, SBDART features a method to adjust the water vapor such that the atmosphere is saturated with respect to liquid water. This method has been updated to saturate the layer with respect to ice if the temperature is below -37°C , and with respect to liquid water above this temperature using the Goff-Gratch equations and assuming water vapor to be an ideal gas. This provides a more realistic intra-cloud environment.

Cloud structure was designed within the simulations such that radiances from both a cirrus cloud with a linearly-increasing extinction coefficient from cloud base to top (i.e., a fallstreak) and a cloud with constant extinction coefficient (i.e., block cloud) were solved independently. The block cloud and fallstreak structures are referred to as ‘infinite-gradient’ and ‘shelf-gradient’ in Bogdanoff et al. (2015), respectively. The modified SBDART simulations showed sensitivity to cloud structure was found to be negligible. Ergo, only results from the fallstreak simulations are presented.

Sensitivity to ice crystal effective radius in SBDART was constrained using the following equation:

$$\begin{aligned}
 D_e &= \alpha e^{\beta T} \quad \text{where,} \\
 \alpha &= 3.084 \times 10^2, \quad \beta = 0.0152 \quad \text{for } -56^\circ < T < 0^\circ C \quad , \\
 \alpha &= 9.171 \times 10^4, \quad \beta = 0.1170 \quad \text{for } -71^\circ < T < -56^\circ C \quad , \\
 \alpha &= 8.330 \times 10^1, \quad \beta = 0.0184 \quad \text{for } -85^\circ < T < -71^\circ C \quad , \quad (3.1)
 \end{aligned}$$

which relates the ice crystal effective diameter (D_e) to cloud temperature (T) as seen in observations of midlatitude ice clouds (Heymsfield et al. 2014). The assumption is made that midlatitude ice particles are identical to tropical ice particles at a similar temperatures. Field experiments into tropical cirrus are difficult due to the extreme altitudes required to sample such clouds, thus, there are no published relationships indicating particle size specifically for tropical cirrus. Ultimately, this equation provides a relationship between SBDART’s standard atmospheric temperature, altitude, and effective radius. Ice crystal effective radius is approximately 95 μm at an altitude of 10 km dropping to near 10 μm by 16 km. Note that there is no normalizing of the actual MODIS/CALIOP contaminated OTC observations as

a function of height/temperature to the temperature profile of the standard atmosphere used to derive the bias values. This will induce some representativeness error in the solutions, since the contaminated observations will not directly coincide with the temperatures and heights of the standard atmosphere. Regardless, as shown in Chapter IV, this error is likely reasonably negligible given that vertical SST bias does not change significantly over scales of only a few hundred meters that this uncertainty would otherwise be relevant.

Sensitivity of the SST error matrices to column water vapor concentrations were tested by adjusting the water vapor mixing ratio profile in the SBDART standard atmosphere during the simulations. Two tests were performed aside from the direct solutions using the standard atmospheric water vapor profile. The first was conducted with the water vapor mixing ratio set to zero everywhere except within the cloud. The other test saturated the entire column with respect to liquid water at temperatures above -37° C and with respect to ice below that temperature. The purpose of this exercise was to provide ample context for considering the integrated bulk SST biases solved from the error matrices, given that the impact of water vapor absorption and column-integrated instrument sensitivities within the SST retrievals themselves can be considerable (e.g., Brown and Minnett 1999).

Observational Representativeness

To characterize the representativeness of the SBDART simulations and corresponding cold bias estimates, an analysis of contaminated MODIS data points is performed for examination of how the calculated bias relates in practice. It is assumed that this is the most practical means to evaluate the skill of the estimates. Advanced Microwave Scanning Radiometer (AMSR) microwave retrieved SSTs, for instance, are not biased by OTC presence, given the much longer wavelength than

IR. Unfortunately, AMSR data are not available for the 2012 study period. Furthermore, AMSR SSTs are retrieved at approximately 25km^2 resolution, causing a lower confidence collocation to finer resolution data from the IR radiometers. To illustrate, single AMSR-retrieved SST pixel can correspond with as many as 625 MODIS pixels. Buoy collocation with MODIS could also be attempted. However, the bias estimates introduced in Chapter IV are, in fact, approximately equal to that found between buoy subsurface temperature measurements and remotely-sensed skin temperature retrievals (Brown and Minnett 1999).

Instead, linear regression is performed between Aqua-MODIS SST retrievals and CALIOP COD for OTC-contaminated retrievals over the Southeast Asian Maritime Continent ($75^\circ\text{E}/15^\circ\text{S} - 135^\circ\text{E}/30^\circ\text{N}$) for August - October 2012. Linear regression over a constrained domain should provide a rough estimate of real world bias imparted by OTC. Thus, a limited spatial and temporal domain was chosen to mitigate any large spatial and seasonal variability, as sample spread limits the effectiveness of the target regressions. This result is qualitatively compared to OTC SST bias estimates derived from the SBDART simulations to gauge how representative the bias estimates are in practice.

CHAPTER IV

ANALYSIS

Collocation Statistics

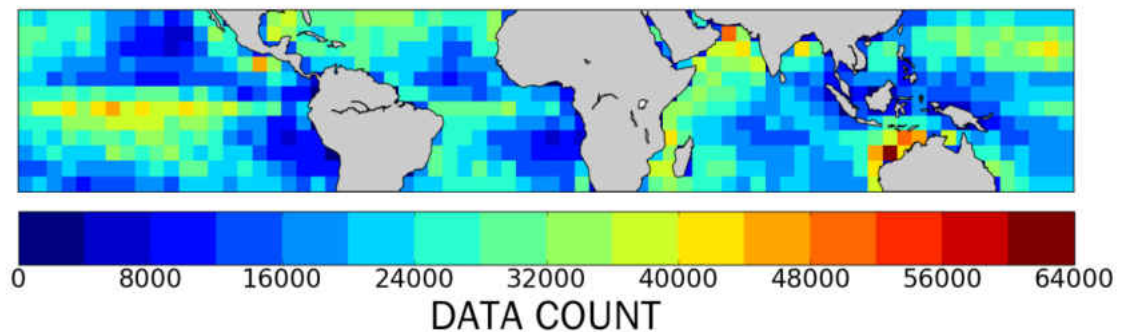


Figure 2: Numbers of collocated Level 2 Aqua-MODIS sea surface temperature (SST) and Level 2 CALIOP cloud-profiling pixels, for MODIS data Quality Levels (QL) 0 and 1, in 5° by 5° bins between 30° S and 30° N.

Although large spatial variation in pixel counts is evident, bins with relatively low collocated Aqua-MODIS/CALIOP data points (such as the Southeast Asian Maritime Continent) still correspond to nearly 10,000 collocated points (Fig. 2). The spatial variability in valid collocations varies both with the availability of QA data, which can be limited due to cloud or other forms of radiance contamination of the MODIS retrieval and OTC occurrence. Comparing Fig. 1 and Fig 2., it is evident that several areas of large OTC occurrence with relatively smaller Aqua-MODIS/CALIOP collocated data counts.

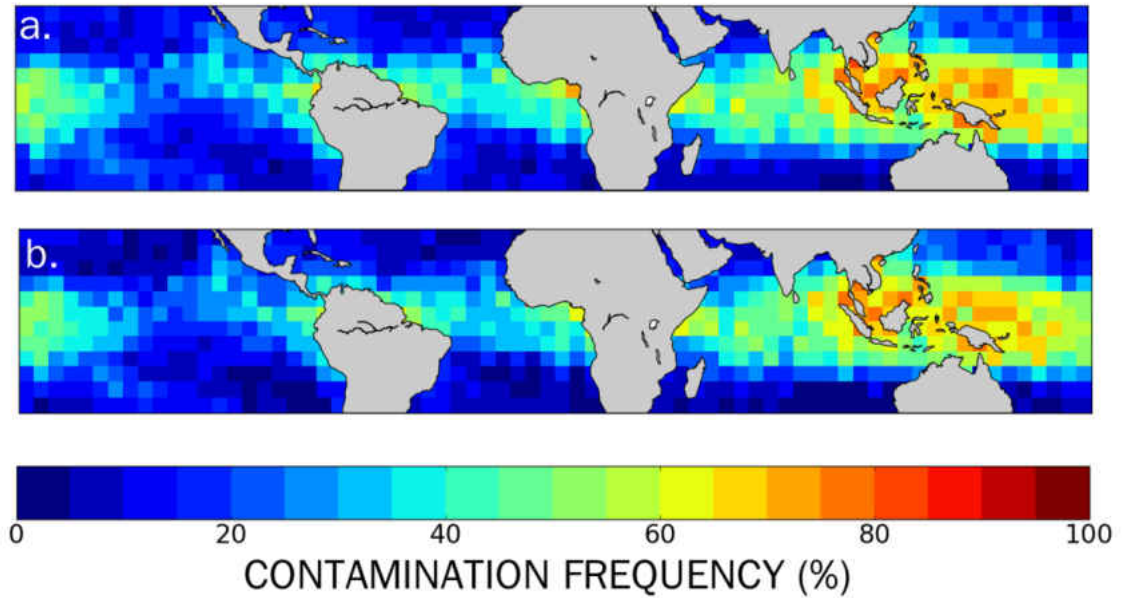


Figure 3: Relative frequencies of collocated Aqua-MODIS SST retrieval contamination, as identified by CALIOP, for a) all cloud, and b) all cirrus (defined as all clouds with a top height temperature -37°C).

Total all-cloud contamination frequencies for the collocated data points bear strong pattern resemblance to observed cirrus occurrence (c.f., Figs 3a and 1a). Of particular interest is the Maritime Continent where cloud is present in upwards of 70% of all collocated data pairs. Comparison of cirrus contamination (Fig. 3b) with all-cloud contamination (Fig. 3a) shows that the majority ($> 90\%$) of all residual cloud is cirrus, though this is likely influenced to some degree by the composition of the Level 2 CALIOP dataset used (i.e., clouds smaller than 5 km are not resolved). Furthermore, 99.4% of the cirrus sample is OTC (25.7% absolute frequency). These distributions and percentages of cirrus contamination closely match expectation (see Fig. 1 and Fig. 1 in Sassen et al. 2008).

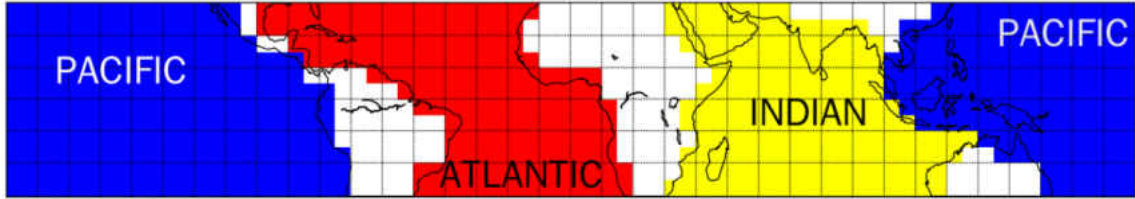


Figure 4: Spatial extent of oceanic basins used in this study, with corresponding 5° by 5° bins depicted from 30° S and 30° N.

Relative contamination characteristics were also investigated (every 5° by 5° bin) with its parent ocean (Fig. 4). Bins that overlap both the Atlantic and Pacific basins, such as bins over Central America and South America, were excluded in the basin investigation. All bins were included, however, between the Indian and Pacific basins because that geographic boundary is not physically well defined and oceanic mixing between those basins occurs in the tropics.

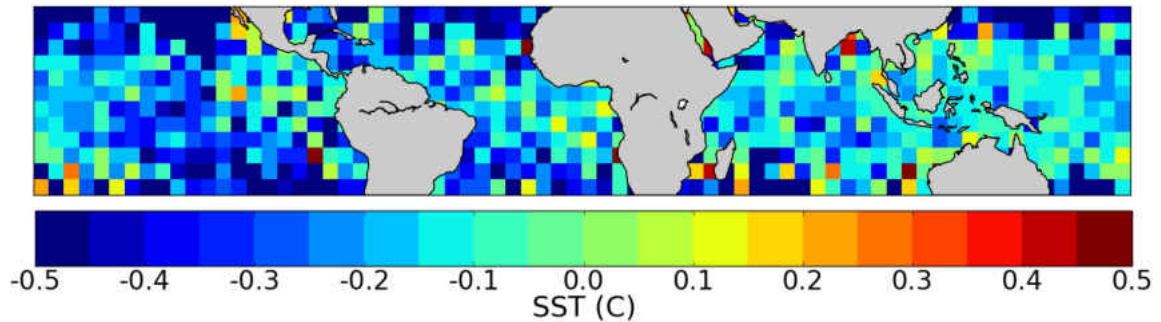


Figure 5: For collocated Aqua-MODIS SST and CALIOP cloud profile data pairs, the absolute difference between the raw QA product and that after cloud screening.

Following in Fig. 5 is the corresponding difference between the cirrus contaminated QA MODIS SST retrievals and those retrievals verified to be clear-sky with CALIOP, whereby the corresponding cold bias effect due to overwhelming OTC presence is first realized. While the majority of all 5° by 5° bins indicate colder cirrus biased retrievals, a small portion of bins indicates that cirrus biased retrievals are warmer than clear-sky retrievals. This discrepancy is likely due to seasonality and

data sampling. While these warm bins do occur in regions of high data count (see Fig. 2), they overwhelmingly occur in regions of low cirrus contamination frequency (see Fig. 3). This results in the mean cirrus contaminated bin SST being indicative of only a few cirrus contaminated retrievals—likely in a localized region of the 5° by 5° bin. Hence, the difference provides a bias that is not indicative of actual retrieval bias within the bin. Accordingly, bins that have high retrieval numbers and moderate to high contamination frequency are all biased cold.

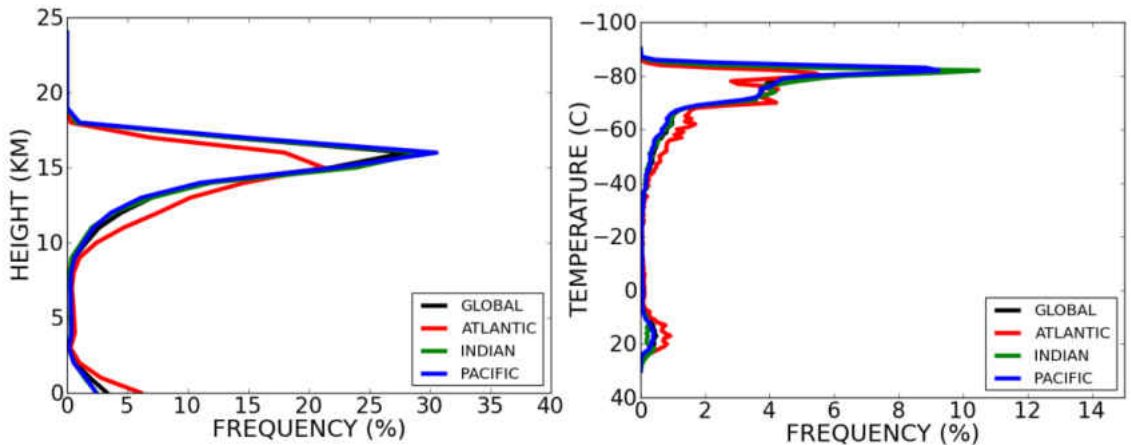


Figure 6: Relative frequencies of all residual cloud found in contaminated Level 2 Aqua-MODIS SST/CALIOP cloud profile data pairs as function of a) cloud top height and b) cloud top temperature, plotted globally and respectively for the Atlantic, Indian and Pacific Ocean basins (see insets).

Histograms of cloud top heights and temperatures for residual clouds identified with CALIOP from the collocated Aqua-MODIS data pairs in each basin are presented in Figs. 6a and 6b, respectively. These plots exhibit a bi-modal distribution between high-altitude cold clouds and near-surface warm clouds, echoing Toth et al. (2013). The Atlantic corresponds with, on average, warmer and lower cloud tops, as well as more low-level cloud contamination than the other oceanic basins. This is likely due to cooler SSTs in the Atlantic, causing lower tropopause heights and lesser influence on ice particle nucleation from the tropical tropopause transition

layer (TTL; Fueglistaler et al. 2009). The TTL is an isothermal layer between the troposphere and the stratosphere. The altitude of this layer is highly dependent on the surface temperature (Fueglistaler et al. 2009). Convective processes within the tropics assist in the formation of TTL cirrus through two mechanisms. First, deep convection can reach the stratosphere causing a cirrus anvil to form within the stable TTL. While this anvil is likely to be optically thick, outflow from the anvil can cause optically thin cloud formation (Jensen et al 1996; Virts 2009). Secondly, synoptic- or planetary-scale waves can result in local ascent. As the air rises, it cools, reaching supersaturation with respect to ice, leading to cirrus formation (Jensen et al 1996; Virts 2009). The Pacific and Indian Oceans exhibit very similar residual cloud properties, which is likely a reflection of both basins sharing the exceptionally warm waters in and around the Maritime Continent.

All basins correspond with a relatively strong residual cirrus signal. Retrieval contamination statistics are outlined in Table 1, distinguished by MODIS retrieval QL and oceanic basin. Here, cirrus contamination refers only to cirrus with no underlying cloud. Globally, the majority of collocations ($>76\%$) were $QL = 0$. These best-quality retrievals still experienced OTC cloud contamination at a rates of nearly 23%, while the lower $QL = 1$ data experienced OTC contamination at approximately 36%. This results in an overall QA dataset OTC contamination rate of roughly 26% throughout the tropics. It is important to note that global analysis is not simply completed by summing the data count for all basins. As previously mentioned, bins that overlapped the Pacific and Atlantic basins are not considered in basin analysis. These bins are, however, considered in the global analysis.

Table 1: Collocated data counts, all-cloud, all-cirrus, and optically-thin cirrus (OTC) contamination statistics calculated from Aqua-MODIS/CALIOP collocation globally and for the Atlantic, Indian and Pacific Ocean basins. Quality control refers to the MODIS Quality Level (QL) 0 and 1 Level 2 dataset used for collocation with CALIOP.

QUALITY		GLOBAL	ATLANTIC	INDIAN	PACIFIC
0	DATA COUNT	11,638,397	2,185,709	2,746,064	5,750,944
	ALL CLOUD CONTAMINATION	24.75%	40.45%	26.81%	27.64%
	CIRRUS CONTAMINATION	22.63%	17.66%	25.06%	25.64%
	OPTICALLY THIN (OTC) FRACTION	99.70%	99.70%	99.75%	99.66%
	MEAN OTC COD	0.034	0.033	0.034	0.034
1	DATA COUNT	3,569,473	701,492	774,006	1,870,591
	ALL CLOUD CONTAMINATION	39.78%	35.62%	43.79%	41.48%
	CIRRUS CONTAMINATION	36.40%	31.47%	40.74%	38.41%
	OPTICALLY THIN (OTC) FRACTION	98.86%	99.15%	98.83%	98.75%
	MEAN OTC COD	0.054	0.047	0.056	0.055
2	DATA COUNT	15,207,870	2,887,201	3,520,070	7,621,535
	ALL CLOUD CONTAMINATION	28.28%	24.14%	30.54%	31.04%
	CIRRUS CONTAMINATION	25.86%	21.01%	28.50%	28.77%
	OPTICALLY THIN (OTC) FRACTION	99.42%	99.50%	99.46%	99.37%
	MEAN OTC COD	0.041	0.038	0.041	0.041

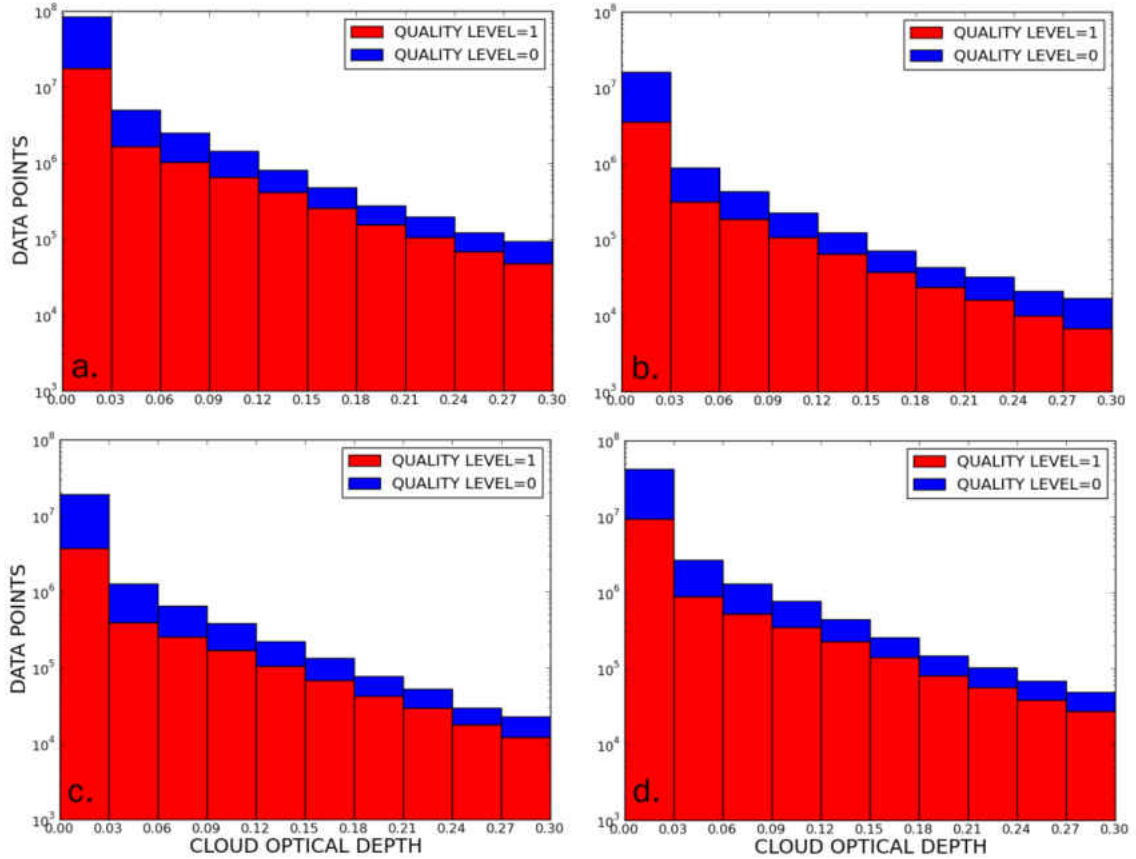


Figure 7: Histograms of residual optically-thin cirrus (OTC) cloud optical depths for Aqua-MODIS SST QL 0 and 1 (see insets) for a) global, b) Atlantic Ocean basin, c) Indian Ocean basin, and d) Pacific Ocean basin.

OTC COD occurrence histograms for contaminated data pairs in each basin are shown in Fig. 7. Similar to OTC distributions derived globally from CALIOP, shown in Campbell et al. (2015), residual COD occurrence across all basins decreases exponentially with increasing COD, with counts in the “sub-visual” range ($COD < 0.03$; Sassen and Cho 1992) occurring two orders of magnitude more often than those approaching the upper-OTC COD threshold near 0.30. Mean contaminating OTC COD globally is near 0.04. This near-sub-visual mean OTC COD is significant in that it validates the assumption that contamination is consistent between MODIS, AVHRR, and VIIRS sensors. Despite generally lower and warmer clouds, the Atlantic

Basin coincides with the optically-thinnest clouds. Additionally, $QL = 1$ clouds were optically thicker than $QL = 0$, as expected. This result is consistent with greater expectation of cloud contamination that would more likely reflect the presence of denser clouds.

Split-Window Bias Estimates

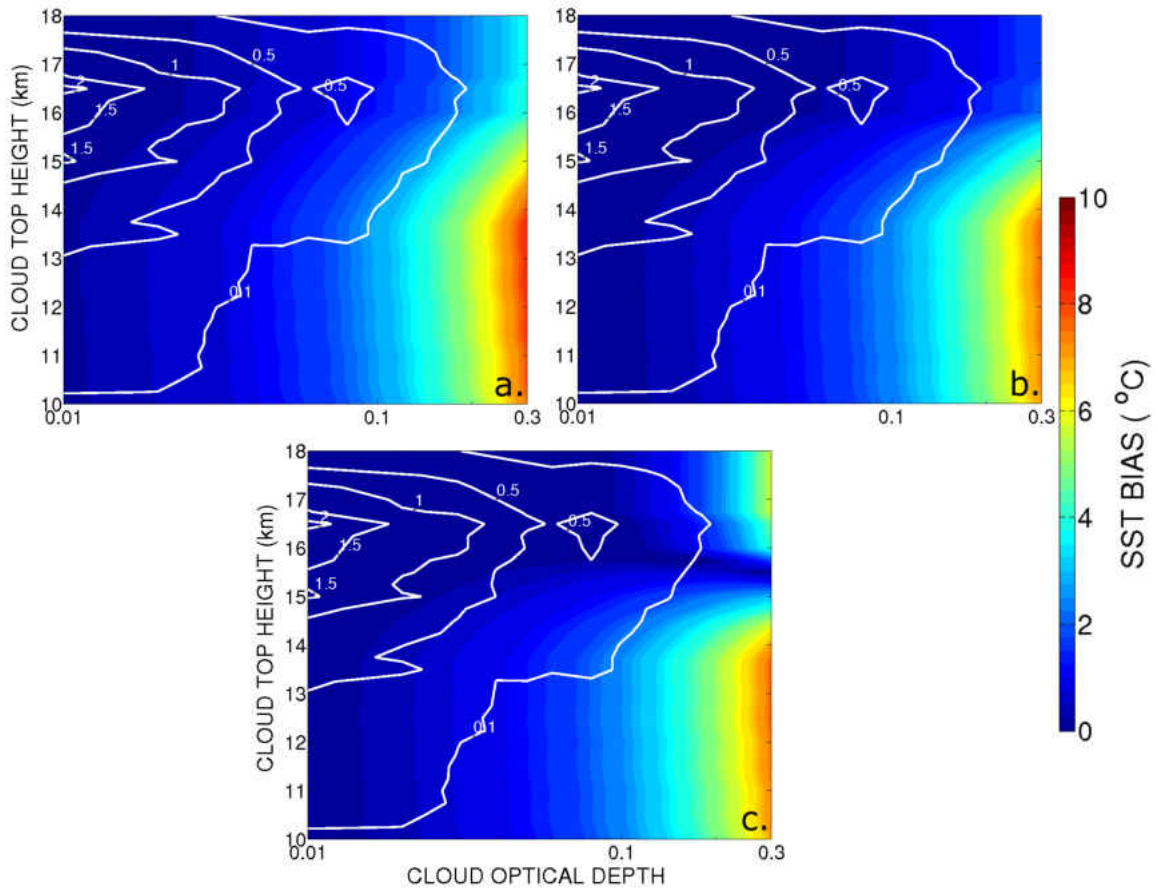


Figure 8: SBDART radiative transfer model simulations of potential SST retrieval cold bias for an unscreened OTC as a function of cloud top height and optical depth for a) MODIS, b) AVHRR, and c) VIIRS. Overlaid on each composite are relative Aqua-MODIS/CALIOP collocated cirrus contamination occurrence frequencies (%).

Respective OTC-only split-window SST cold bias matrices are shown in Fig. 8 for (a) Aqua-MODIS, (b) AVHRR and (c) VIIRS. Overlaid on these data are

relative occurrence percentages of cloud contamination from Aqua-MODIS/CALIOP. As described in Chapter III, only single-layered OTC bias is solved. Therefore, the range of cloud top altitudes (10 - 18 km) are only meant to simulate OTC. The 10 km minimum altitude corresponds to -37° C, which is defined as the maximum cloud top temperature for cirrus distinction. The magnitude of bias for each cloud type is given by the color-filled contours. For example, a cloud with cloud top altitude of 14 km and COD of 0.10 has a solved cold bias of approximately 3° C for all sensors. White contours indicate the global relative frequency of occurrence of each cloud type bin. To demonstrate, a cloud with cloud top altitude at 16.5 km and COD of 0.01 occurs in approximately 2% of all OTC contaminated retrievals. Thus, net OTC cold bias estimates are solved by integrating the product of relative and absolute frequencies of cloud type occurrence and corresponding bias at each bin as functions of cloud top height and COD. Again, it is emphasized for AVHRR and VIIRS that this step assumes OTC cloud clearing algorithm infidelities are reasonably consistent across each sensor.

The SBDART simulations, and thus all corresponding bias estimates, were only conducted for the nadir view of either sensor. Assuming that OTC contamination occurrence rates are relatively consistent at all viewing angles as a function of COD, an expanded study could take into account varying passive sensor response to viewing angle. However, given the complexities of passive cloud screening algorithms, such as “buddy check” pixel comparisons, the assumption that occurrence rates are consistent at all viewing angles is likely a poor assumption. Furthermore, relative COD effectively increases with greater viewing angle due to increased optical path length, clouds of lower absolute COD may be better screened at non-nadir viewing angles. With that said, most of the residual cloud was approaching sub-visual distinction. Given the increases in relative COD due to viewing geometry, these clouds

may still be undetectable. In that case, cold bias may increase at non-nadir viewing angles.

Evident in the cold bias simulations is sensitivity to both altitude, and, thus, cloud temperature and ice effective radius. Despite this, there is arguably larger sensitivity to COD (i.e., ice water path). Each sensor retrieval algorithm exhibits generally negligible bias at sub-visual COD ($\text{COD} \leq 0.03$; Sassen and Cho 1992). All sensors exhibit maximum bias at CODs approaching 0.3 and cloud top altitudes below 15 km, corresponding with effective cloud particle radii greater than $25 \mu\text{m}$. This maximum indicates bias greater than 8°C for MODIS retrievals and greater than 6°C for AVHRR and VIIRS retrievals. Above 15 km (ice effective radius $< 25 \mu\text{m}$), both MODIS and AVHRR exhibit smaller retrieval biases, near approximately 4°C and 2°C respectively. VIIRS, however, exhibits a secondary maximum above 16 km, approaching 6°C . This secondary maximum is presumably due to VIIRS exhibiting increased sensitivity to smaller effective radii near $10 \mu\text{m}$ than the other sensors, reflecting slight differences in sensor spectral response, retrieval wavelength, and retrieval algorithms themselves.

Cold bias estimates are reported in Tables 2 and 3 for each sensor, based upon Aqua-MODIS QL and oceanic basin. Ranges of bias associated with water vapor sensitivity are also reported according to the supplemental experiments described in Chapter III. The mean absolute global QA OTC-only SST cold bias estimated across the three platforms from these simulations without varying the relative humidity profile from that of the standard atmosphere is between 0.10 and 0.13°C . This range reflects the absolute aggregate cold bias estimated for each sensor in bulk-average tropical SST, given OTC-only contamination occurrence rates on the order of 25%. The corresponding relative bias ranges from 0.40 - 0.49°C , reflecting the mean cold bias specifically for OTC-contaminated single observations. AVHRR and MODIS

Table 2: Mean absolute, or bulk mean, OTC cold biases in MODIS, AVHRR, and VIIRS SST split-window retrievals from SBDART simulations and assuming Aqua-MODIS/CALIOP collocated contamination frequencies, segregated as function of QL, global and Atlantic, Indian and Pacific Ocean basins. Absolute OTC cold biases for atmospheric profile with no water vapor and saturated column are given in parentheses, respectively.

SENSOR	QL	GLOBAL (° C)	ATLANTIC (° C)	INDIAN (° C)	PACIFIC (° C)
MODIS	0	0.09 (0.06 - 0.13)	0.08 (0.06 - 0.11)	0.10 (0.06 - 0.15)	0.10 (0.06 - 0.15)
	1	0.24 (0.18 - 0.34)	0.21 (0.17 - 0.28)	0.28 (0.20 - 0.39)	0.13 (0.09 - 0.19)
	QA	0.13 (0.09 - 0.18)	0.08 (0.08 - 0.10)	0.10 (0.09 - 0.13)	0.10 (0.09 - 0.13)
AVHRR	0	0.09 (0.09 - 0.11)	0.08 (0.08 - 0.10)	0.10 (0.09 - 0.13)	0.10 (0.09 - 0.13)
	1	0.24 (0.23 - 0.29)	0.21 (0.20 - 0.25)	0.28 (0.26 - 0.34)	0.24 (0.22 - 0.30)
	QA	0.13 (0.12 - 0.16)	0.11 (0.11 - 0.13)	0.14 (0.13 - 0.17)	0.13 (0.12 - 0.17)
VIIRS	0	0.07 (0.25 - 0.22)	0.07 (0.19 - 0.17)	0.08 (0.29 - 0.24)	0.08 (0.29 - 0.25)
	1	0.21 (0.56 - 0.54)	0.18 (0.45 - 0.44)	0.23 (0.66 - 0.60)	0.20 (0.60 - 0.57)
	QA	0.10 (0.32 - 0.30)	0.09 (0.25 - 0.24)	0.11 (0.37 - 0.32)	0.11 (0.36 - 0.33)

Table 3: As in Table 2, but for mean relative, or per contaminated observation, cold biases.

SENSOR	QL	GLOBAL (° C)	ATLANTIC (° C)	INDIAN (° C)	PACIFIC (° C)
MODIS	0	0.40 (0.27 - 0.59)	0.45 (0.33 - 0.62)	0.40 (0.26 - 0.60)	0.38 (0.34 - 0.57)
	1	0.66 (0.48 - 0.92)	0.68 (0.53 - 0.90)	0.68 (0.49 - 0.96)	0.62 (0.44 - 0.90)
	QA	0.49 (0.34 - 0.70)	0.53 (0.40 - 0.72)	0.49 (0.33 - 0.71)	0.46 (0.30 - 0.67)
AVHRR	0	0.40 (0.38 - 0.51)	0.45 (0.42 - 0.54)	0.40 (0.38 - 0.51)	0.68 (0.35 - 0.49)
	1	0.66 (0.62 - 0.80)	0.68 (0.65 - 0.79)	0.68 (0.64 - 0.83)	0.62 (0.59 - 0.78)
	QA	0.49 (0.45 - 0.60)	0.53 (0.51 - 0.63)	0.49 (0.46 - 0.61)	0.46 (0.43 - 0.58)
VIIRS	0	0.32 (1.11 - 0.97)	0.37 (1.08 - 0.97)	0.31 (1.14 - 0.96)	0.29 (1.11 - 0.97)
	1	0.57 (1.55 - 1.49)	0.59 (1.44 - 1.40)	0.57 (1.62 - 1.48)	0.53 (1.56 - 1.50)
	QA	0.40 (1.25 - 1.14)	0.44 (1.21 - 1.13)	0.39 (1.29 - 1.12)	0.37 (1.26 - 1.15)

biases are identical and approximately 20% greater than VIIRS. Relative cold biases are, of course, greater, reflecting the impact of a single event as opposed to an event normalized by its absolute occurrence rates.

Water vapor sensitivity is relatively stable across MODIS and AVHRR, with AVHRR exhibiting slightly less variance than MODIS. Values derived for the perturbed water vapor mixing ratio profiles relative to the standard atmosphere encompass the two sets simulations as lower and upper bounds, respectively ($0.09^\circ - 0.18^\circ$ C and $0.12^\circ - 0.16^\circ$ C absolute and $0.34^\circ - 0.70^\circ$ and $0.45^\circ - 0.60^\circ$ C relative, respectively). VIIRS results differ significantly, exhibiting a range of values much greater than the unperturbed case ($0.32^\circ - 0.30^\circ$ C absolute and $1.25^\circ - 1.14^\circ$ C relative, respectively). This result indicates that the VIIRS algorithm has undergone some specific tuning that limits skill in the event that OTC presence corresponds with a relatively unnatural water vapor profile. This unusual result requires further investigation.

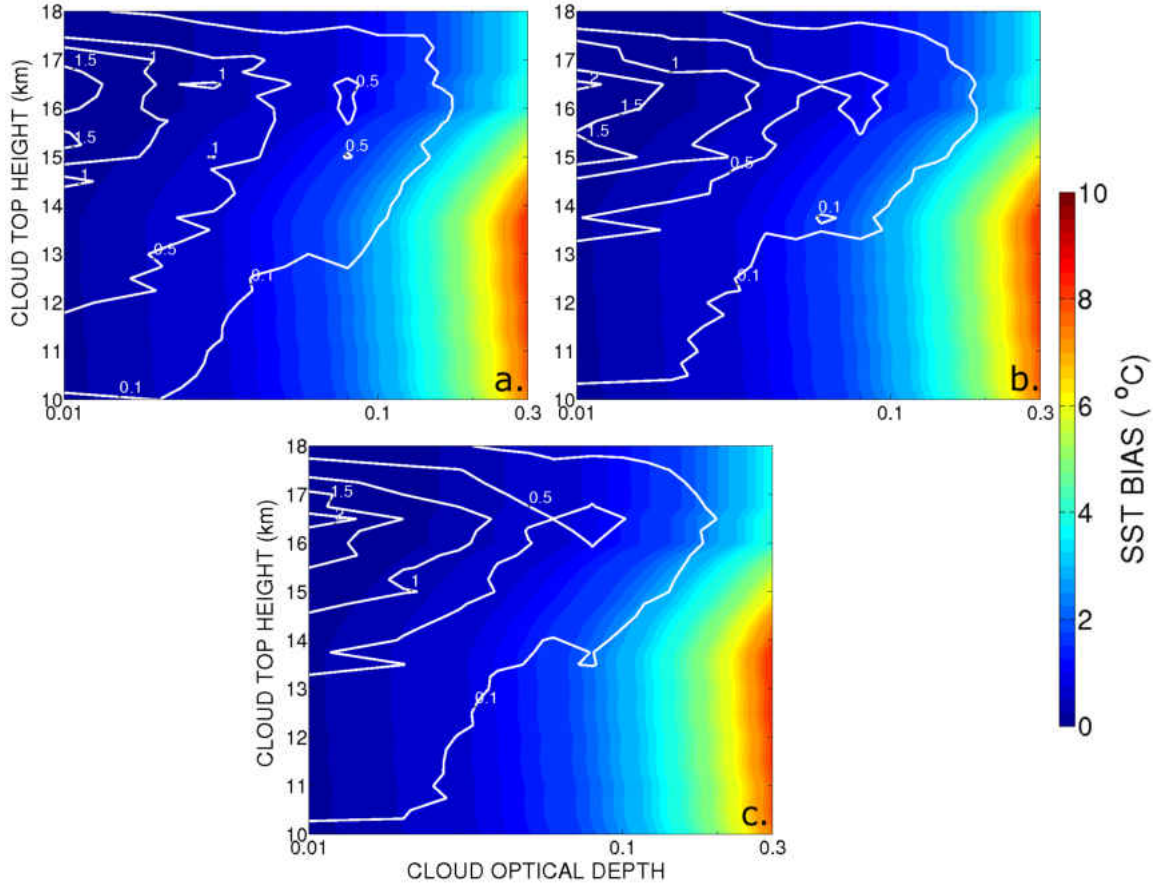


Figure 9: As in Fig. 8, now for MODIS only over the a) Atlantic, b) Indian and c) Pacific Ocean basins.

Figure 9 features MODIS-only cold bias composites and relative OTC contamination rates for the (a) Atlantic, (b) Indian, and (c) Pacific Ocean basins, respectively (see basins in Fig. 4). Again, the Indian and Pacific Ocean basins exhibit relatively similar distributions, with the Atlantic Ocean profile being much more broadly distributed in terms of relative percentage frequency with height. Note that some under-sampling in the absolute/relative OTC cold bias estimates derived from these data arises, and is apparent in both Figs. 8a-c and 9a-c with occurrence contours showing clouds present above 18 km. SBDART simulations were only conducted between 10.0 and 18.0 km. The lower threshold coincides approximately with -37° C on the tropical

standard atmospheric profile used in SBDART, which is the thermal threshold used to distinguish cirrus clouds in the CALIOP sample (described in Chapter II). The upper threshold (18 km) is actually 0.5 km above the cold-point tropopause height in the standard atmospheric profile used—meaning clouds above 17.5 km occur within the tropopause in the standard atmosphere used for the simulations. Nonetheless, it is relatively common to see cirrus clouds in the tropics, particularly TTL cirrus, to and above 18.0 km (e.g., Campbell et al 2015, among many others). This upper threshold was adjusted slightly from the standard atmosphere cold-point tropopause accordingly. Reality, however, causes some cirrus (specifically OTC) to be observed by CALIOP outside of this range within the tropics, which are included in the OTC-contaminated Aqua-MODIS/CALIOP sample. Ultimately, 1.07% of the tropical OTC sample is not accounted for when integrating the cold bias matrices and deriving final estimates because it falls outside of the 10 - 18 km bounds of the simulation. Therefore, the resulting biases may be slightly low. Combined with the assumptions discussed in Chapter III, it is reiterated that these solutions are strictly estimates.

Absolute/relative cold bias estimates for the Indian and Pacific Ocean basins are relatively constant across the three sensors, as seen in Tables 2 and 3. In contrast, the absolute cold bias is smaller over the Atlantic Ocean due to less frequent OTC occurrence. It is important to note that, while having lower absolute bias, the Atlantic basin exhibits the largest relative bias. This is a direct result of the lower and warmer OTC in this basin. As previously mentioned, these differences in OTC properties are likely due to cooler surface temperatures and a lower TTL. Thus, the results from the Atlantic may also be indicative of the expected results outside of the tropics. At higher latitudes, cirrus frequency will drop, yet, the bias associated with each cirrus cloud will be greater. This presents not only a problem for SST retrieval in the tropics, but at all latitudes globally.

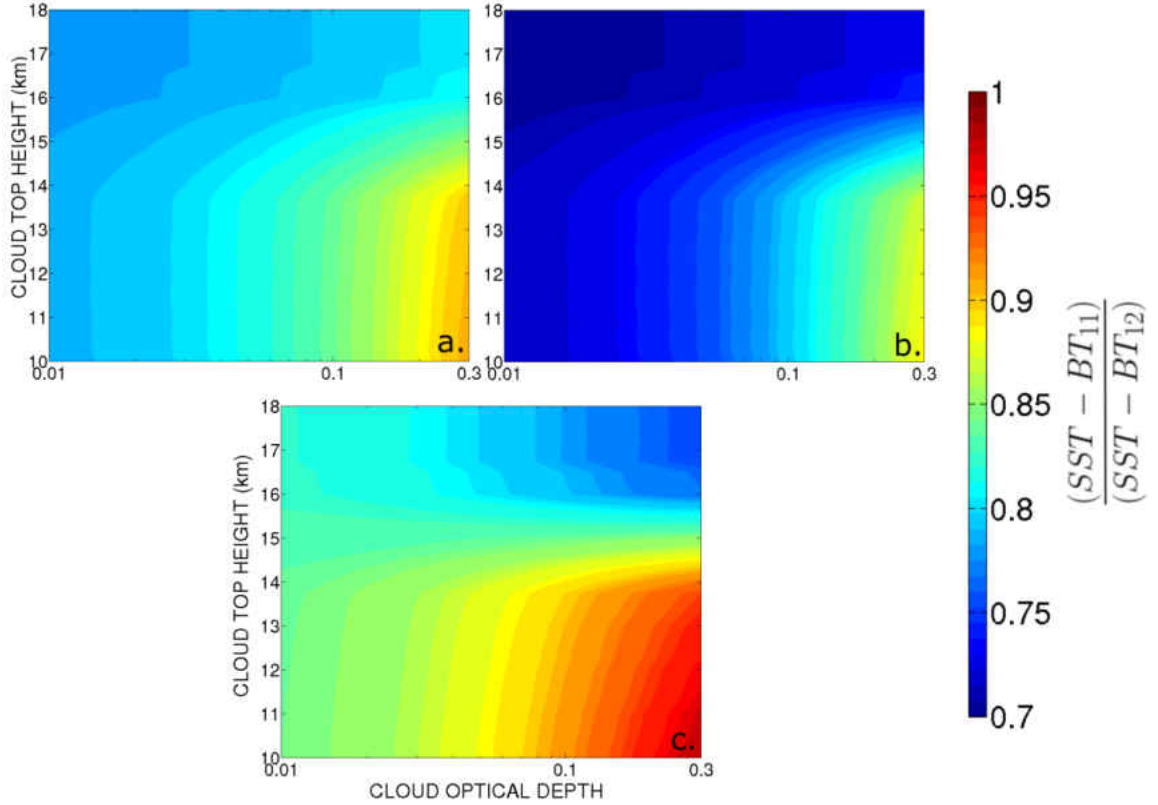


Figure 10: SBDART radiative transfer model simulations of the ratio of the difference between the clear sky retrieved SST and the OTC-contaminated 11 and 12 μm brightness temperatures as a function of cloud top height and optical depth for a) MODIS, b) AVHRR, and c) VIIRS split-window algorithms.

Figure 10 depicts the ratio of the difference between the retrieved clear-sky SST and the OTC-contaminated brightness temperatures modeled for each sensor in SBDART from the corresponding near-11 and near-12 μm bands. Since split-window algorithms are based upon the assumption that these differences are proportional and constant, Figure 10 should theoretically show no change for different cloud properties (i.e., the figures should be a solid color). However, the significant variance depicted in each sensor illustrates a failure of the developmental assumptions of split-window algorithms in the presence of cloud. A similar response was illustrated by Merchant et al. (1999) for stratospheric volcanic aerosols. MODIS exhibits the least vari-

ance here, with proportionality ranging from approximately 0.8 to 0.9, while AVHRR ranges from approximately 0.7 to 0.9. The largest variance is seen in the VIIRS simulations, with the ratio of proportionality ranging from 0.7 to 1.0. The ratio in VIIRS also exhibits a minimum at CODs approaching 0.3 above 15 km. This minimum corresponds to the secondary maximum in SST retrieval bias caused by sensor sensitivity to relatively small effective cloud particle radii.

Triple-Window Bias Estimates

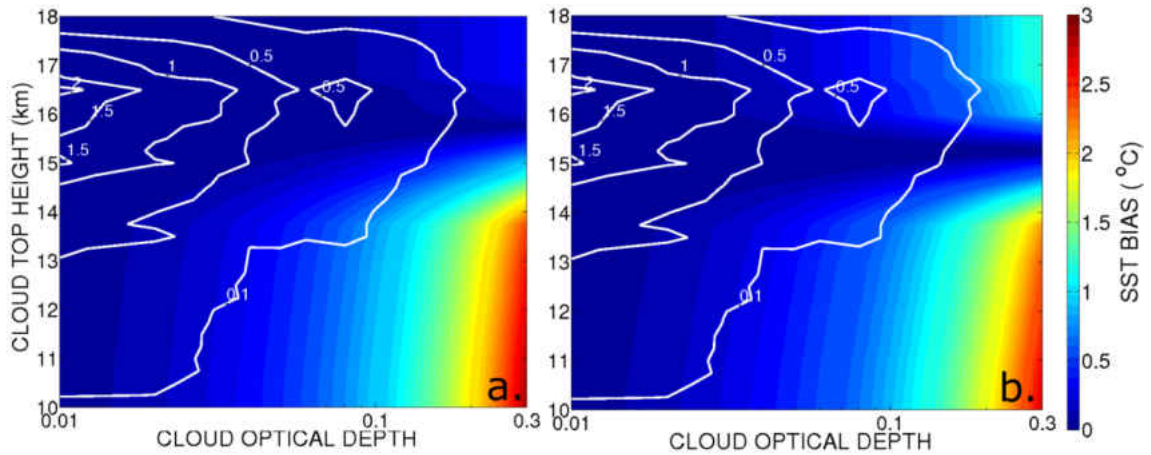


Figure 11: SBDART radiative transfer model simulations of potential triple-window SST retrieval cold bias for an unscreened OTC as a function of cloud top height and optical depth for a) AVHRR, and b) VIIRS. Overlaid on each composite are relative Aqua-MODIS/CALIOP collocated cirrus contamination percentage occurrence frequencies (%).

Triple-window OTC cold bias matrices and absolute and relative bias estimates for AVHRR and VIIRS are presented in Figure 11 and Table 4. Again, to the author’s knowledge, there is no operational MODIS triple-window product publicly available. Bias structure is similar to the split-window for both sensors, though the AVHRR simulations now exhibit the secondary maximum in bias above 15 km, similar to VIIRS split-window (albeit at lower magnitudes). The triple-window al-

Table 4: Mean absolute (relative) OTC cold biases in MODIS, AVHRR, and VIIRS SST triple-window retrievals from SBDART simulations and assuming Aqua-MODIS/CALIOP collocated contamination frequencies, segregated as function of QL, global and Atlantic, Indian and Pacific Ocean basins.

SENSOR	QL	GLOBAL (° C)	ATLANTIC (° C)	INDIAN (° C)	PACIFIC (° C)
AVHRR	0	0.02 (0.09)	0.02 (0.10)	0.02 (0.08)	0.02 (0.08)
	1	0.05 (0.15)	0.05 (0.16)	0.06 (0.15)	0.05 (0.14)
	QA	0.03 (0.11)	0.03 (0.12)	0.03 (0.10)	0.03 (0.10)
VIIRS	0	0.03 (0.14)	0.02 (0.14)	0.03 (0.13)	0.03 (0.14)
	1	0.07 (0.21)	0.06 (0.20)	0.08 (0.21)	0.08 (0.21)
	QA	0.04 (0.16)	0.03 (0.16)	0.04 (0.16)	0.05 (0.16)

gorithms are less susceptible to cirrus contamination than split-window in terms of bias magnitude. This may be due to the algorithms basing more weight upon the 3.7 μm observation, or basically, the use of more information for retrieval (3 bands vs. 2 bands in split-window retrievals).

Global AVHRR absolute and relative biases are estimated at 0.03°C and 0.11°C , respectively. Unlike split-window, these global biases are smaller than VIIRS (0.04°C absolute and 0.16°C relative). Bias estimates drop $> 60\%$ for VIIRS and $> 75\%$ for AVHRR, overall. Thus, triple-window techniques exhibit much greater resilience to OTC, in spite of operational limitations to nighttime use only in all practical circumstances. This is due to solar reflectance contaminating the 3.7 μm retrieval during daylight, as explained in Chapter II. With relative bias ranging from 0.10°C to 0.16°C across all basins and sensors, the triple-window product is significantly more stable for operational use than split-window. Due to the relatively small bias

estimates solved, and considering issues encountered with VIIRS above, a water vapor sensitivity analysis was not performed.

Verification

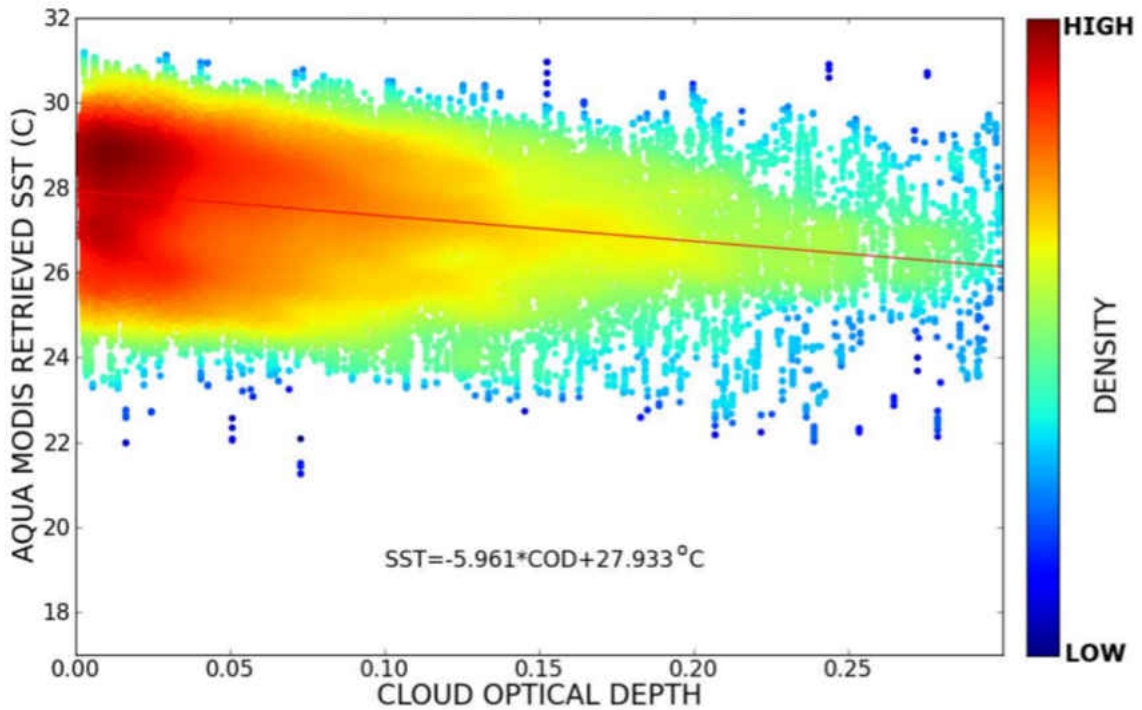


Figure 12: Scatter plot of CALIOP cloud optical depth versus Aqua-MODIS SST from OTC-contaminated retrievals for August - October 2012 over the Maritime Continent (75°W/15°S - 135°W/30°N).

To gauge the representativeness of the SBDART-modeled OTC cold bias estimates, comparison with available observations was performed. Figure 12 depicts a scatter plot of OTC-contaminated SST vs. COD over the Southeast Asian Maritime Continent (75°E/15°S - 135°E/30°N) for August - October 2012. This area was selected specifically due to extremely high frequency of OTC occurrence compared to the rest of the tropics. Thus, sample variance could be constrained with the least amount of data lost. The premise is that the slope of a linear regression fit to

these data should approximately equal the relationship between cold bias and OTC COD estimated from Fig. 8. The slope solved from these data is -6° C per COD, or approximately 1.8° C per 0.30 COD. Conversely, Figure 8 depicts a range of cold biases with height varying between 8° C to 4° C at 0.30 COD, with 4° C corresponding to the altitude where most OTC are present.

Though the observational bias seen in the regression is approximately 50% smaller than the modeled bias, there is reason to believe that this is a wholly practicable comparison. First, there is significant SST variance within the sample, despite efforts to constrain the variance in time and space. The primary mode of points are aggregated near 29° C approaching 0.00 COD, though values range between 24° and 31° C overall. Further, effects of MODIS QL and data rejection are present at the high COD end of the sample. MODIS QL is based on deviation from a background/*a priori* temperature. In other words, while the upper bound of observations has a definite slope of approximately $3 - 4^{\circ}$ C per 0.30 COD, the lower bound of observations is flat or sloping slightly upwards. The reason for this upward slope in the lower bound is likely background temperature deviation tests used in determination of the QL. While warm retrievals biased cold will pass the less than 3° C distinction between background and retrieved SST required to be $QL < 2$, cold retrievals biased colder will not pass. Thus, both effects are contributing to the regression slope, in opposing ways (biased low on cool SST end and high on warm end), which are acting to reduce its relative value compared with the model. At any rate, distinguishable evidence of the effect in these data alone is encouraging.

CHAPTER V

CONCLUSIONS

Unscreened cloud contamination within the Level 2 Aqua Moderate Resolution Imaging Spectroradiometer (MODIS) split-window infrared (IR) sea surface temperature (SST) retrievals at instrument nadir in the tropics (MOD28; 30°S - 30°N) during 2012 is characterized through collocation with Version 3 Level 2 5-km cloud profiles from the Cloud Aerosol Lidar with Orthogonal Polarization (CALIOP) instrument. Specifically, optically-thin cirrus (OTC; cloud optical depths ≤ 0.30 ; COD) cloud contamination is highlighted for its predominant contribution to total cloud contamination of passive IR radiometric retrievals corresponding with previous findings (e.g., Holz et al. 2008). Clouds of any type were found in approximately 28% of all Level 2 Aqua-MODIS data characterized as Quality Level (QL) 0 or 1 (denoted as QA), used for quality control dataset characterization. These estimates may be biased low given that the specific 5-km cloud product used from CALIOP ignores cloud samples resolved at finer resolutions. Of the contaminating cloud, greater than 90% is cirrus (25.96% absolute) and 99.4% of the contaminating cirrus (25.7% absolute) is OTC, with the remaining clouds being mostly low and warm near-surface liquid water clouds. Such a bi-modal residual cirrus/low cloud distribution was also found to contaminate the MODIS aerosol optical depth product (Toth et al. 2013).

OTC contamination characteristics from collocated Aqua-MODIS/CALIOP data pairs are used to estimate corresponding split-window IR SST retrieval cold biases for MODIS, Advanced Very High Resolution Radiometer (AVHRR), and the

Visible Infrared Imaging Radiometer Suite (VIIRS), as well as triple-window retrievals in AVHRR and VIIRS. Respective SST retrievals are modeled using the Santa Barbara DISORT Atmospheric Radiative Transfer model (SBDART), equipped with an advanced ice crystal microphysical parameterization and optical scattering properties (Yang et al. 2005; Heymsfield et al. 2014).

Two-dimensional OTC-contaminated SST retrieval cold bias matrices are solved for both the split- and triple-window IR algorithms after simulating the retrievals using a tropical standard atmosphere and the presence of a hypothetical OTC layer (1.5 km thick) between 10.0 and 18.0 km cloud top height above mean sea level (solved in 0.25 km segments) and COD between 0.00 and 0.30 (in 0.01 segments from 0.01 - 0.06 and 0.02 segments above 0.06). Simulations were performed using both a cloud structured with a constant optical extinction coefficient (“block cloud”) and one with a linearly-decreasing extinction coefficient value from cloud top to cloud base of five-to-one (“fallstreak”). Having found very little difference in the results, only fallstreak results are presented in this study. Relative and absolute OTC SST cold biases were, then, estimated by multiplying the corresponding instrument matrix by the corresponding occurrence frequency of OTC occurrence as a function of height and COD estimated from the Aqua-MODIS/CALIOP comparisons.

The mean absolute global split-window OTC SST cold bias estimated across the MODIS, AVHRR, and VIIRS platforms from these simulations using a standard atmosphere profile is between 0.10° and 0.13° C using QA Aqua-MODIS/CALIOP contamination characteristics, with a corresponding global contamination occurrence rate near 25%. The relative bias ranges from 0.40° to 0.49° C from OTC alone. Relative cold biases are greater, reflecting the impact of a single contamination event as opposed to one normalized by its absolute occurrence rates. AVHRR and MODIS biases are nearly identical and significantly greater than VIIRS. After varying the

water vapor mixing ratio profile between completely dry (except within the modeled OTC cloud) to liquid water and ice saturated, MODIS varies from $0.09^\circ - 0.18^\circ$ C absolute and $0.34^\circ - 0.70^\circ$ relative. AVHRR varies from $0.12^\circ - 0.16^\circ$ C absolute and $0.45^\circ - 0.60^\circ$ C relative, respectively. In VIIRS, however, the result was significantly different— $0.32^\circ - 0.30^\circ$ C absolute and $1.25^\circ - 1.14^\circ$ C relative, which requires subsequent reconciliation.

Triple-window simulations show an improved response to OTC presence, though these retrievals may only be performed with reasonable expectation during night due to the increased potential for contamination of the shortwave IR band used. AVHRR global QA OTC SST bias is estimated at 0.03° C absolute and 0.11° C relative, while VIIRS exhibits slightly degraded performance at 0.04° C absolute and 0.16° C relative. The triple-window algorithm is significantly more resilient to OTC presence than split-window, in spite of its limited diurnal use.

Both split-window and triple-window results are relatively constant across the Indian and Pacific Ocean basins, owing to relatively common cirrus cloud macro-physical properties. Absolute cold biases are smallest over the Atlantic Ocean, corresponding with lower overall cirrus frequency. However, relative cold biases are actually greater in the Atlantic, owing to lower-topped OTC regionally that correspond with larger effective cloud top ice crystal radii that are increasingly more active IR emitters compared with smaller/colder/higher OTC elsewhere. This result leads to the conclusion that OTC SST bias is likely to persist significantly moving poleward from the tropics, despite lower regional occurrence frequencies. Consistency of the difference between the clear-sky split-window SST and OTC-contaminated brightness temperature from the near-11 and near-12 μm bands in MODIS, AVHRR, and VIIRS is also presented in this study, depicting the failure of developmental assumptions in the presence of OTC.

Sources of uncertainty relating to these OTC SST cold bias modeling estimates are described. First, cloud contamination characteristics are uniquely extrapolated from Aqua-MODIS/CALIOP data pairs to AVHRR and VIIRS. Cold bias estimates for these latter two sensors are, thus, practical estimates based on this assumption of continuity in OTC contamination between the three passive IR radiometric sensors. Second, the SBDART simulations were conducted only between 10.0 and 18.0 km. The 10.0 km altitude coincides with the -37° C level in the standard atmosphere profile used by the model that helps discriminate cloud tops in the Aqua-MODIS/CALIOP collocated dataset for cirrus cloud presence (Campbell et al. 2015). The 18.0 km altitude is 0.5 km above the corresponding cold point tropopause in the standard atmosphere profile—extended slightly to account for tropical tropopause transition layer (TTL) cirrus cloud presence. In reality, 98.93% OTC cloud top heights found from the Aqua-MODIS/CALIOP data pairs fell within this altitude range, meaning that the integrated absolute/relative cold bias estimates are slightly low.

Further uncertainty arises from the use of a static tropical standard atmosphere and static surface SST in deriving the cold bias matrices utilizing the SBDART radiative transfer model. Importantly, the Aqua-MODIS/CALIOP-contaminated observations were not normalized for height/temperature to the standard atmosphere before integrating the absolute/relative cold bias estimates for simplicity. Since there is little relative variability in OTC SST cold bias with height, for which we consider this effect relevant, this uncertainty is expected to be relatively small. Finally, there is slight underestimation of bias due to multilayered cloud scenes. Bias was solved using only single-layered OTC scenes. Scenes with multiple layers of cloud would result in more bias due to the higher column COD, which is shown in this study to have higher effect on bias than cloud top altitude. The impact of uncertainties in the base CALIOP Level 2 COD product are also described, and the effect is believed negligible

given that the accuracy of these values is typically optimal within optically-thinner clouds.

The community faces a continuing issue with respect to the use of passive remote sensors for operational meteorological and oceanographic measurements: cirrus clouds are the most common cloud genus in the atmosphere and cloud detection algorithms built off of passive radiances struggle to find OTC that make up roughly half of all cirrus clouds. With global occurrence rates of 40-60% (Mace et al. 2009), cirrus, and particularly OTC clouds, represent a significant and binding “noise” to passive retrievals that require careful and considerate error characterization for a host of ongoing applications.

This paper provides a reasonable and novel set of guidelines for more accurately constraining relative uncertainties in operational SST retrieval products. In the bigger picture, as new missions are planned and gradually come on line, it is becoming increasingly incumbent upon the scientific community to find practical solutions for suppressing OTC contamination of passive IR radiometric Level 2 datasets. Whether that means pairing passive satellite sensors with simple/inexpensive lidar profilers, adding of additional infrared bands, or finding advanced spectral analysis methods (e.g., Gao et al. 1998) for improved OTC discrimination, unless the community is willing to accept an uncertainty that cannot effectively be *seen* passively from space, this problem will continue to persist (e.g., Huang et al. 2016).

APPENDICES

Appendix A
List of Abbreviations

Table 5: List of Abbreviations

Abbreviation	Full Text
AC-SPO	Advanced Clear-Sky Processor for Oceans
AERONET	AERosol RObotic NETwork
AMSR	Advanced Microwave Scanning Radiometer
AVHRR	Advanced Very High Resolution Radiometer
CALIPSO	Cloud-Aerosol LiDAR and Infrared Pathfinder Satellite Observation
CALIOP	Cloud-Aerosol LiDAR with Orthogonal Polarization
COD	Cloud Optical Depth
ENSO	El Niño-Southern Oscillation
GMAO	Goddard Model Assimilation Office
GOES	Geostationary Operational Environmental Satellite
IR	Infrared
LiDAR	Light Detection and Ranging
MODIS	MODerate resolution Imaging Spectroradiometer
NASA	National Aeronautics and Space Administration
NAVO	Naval Oceanographic Office
NLSST	Nonlinear SST
NOAA	National Oceanographic and Atmospheric Administration
NPP	National Polar-orbiting Partnership
OISST	Optimum Interpolation Sea Surface Temperature
OTC	Optically Thin Cirrus
QA	Quality Assured
QL	Quality Level
SBDART	Santa Barbara DISORT Atmospheric Radiative Transfer
SST	Sea Surface Temperature
TC	Tropical Cyclone
TTL	Tropical Tropopause Layer
VIIRS	Visible-Infrared Imaging Spectroradiometer

REFERENCES

- Barton, I.J., 1995: Satellite-derived sea surface temperatures: Current status. *J. Geophys. Res.*, **100**, 8777-8790.
- Bogdanoff, A. S., D. L. Westphal, J. R. Campbell, J. A. Cummings, E. J. Hyer, J. S. Reid, C. A. Clayson, 2015: Sensitivity of infrared sea surface temperature retrievals to the vertical distribution of airborne dust aerosol. *Remote Sens. Environ.*, **159**, 1-13.
- Brisson, A., P. Le Borgne, and A. Marsouin, 2002: Results of one year of preoperational production of sea surface temperatures from GOES-8. *J. Atmos. Oceanic Technol.*, **19**, 1638-1652.
- Brown, O. B. and Minnett, P. J., 1999: MODIS Infrared Sea Surface Temperature Algorithm Theoretical Basis Document Version 2.0. *University of Miami*.
- Campbell, J. R., M. A. Vaughan, M. Oo, R. E. Holz, J. R. Lewis, and E. J. Welton, 2015: Distinguishing cirrus cloud presence in autonomous lidar measurements. *Atmos. Meas. Tech.*, **8**, 435-449.
- Chew, B. N., J. R. Campbell, J. S. Reid, D. M. Giles, E. J. Welton, S. V. Salinas, S. C. Liew, 2011: Tropical cirrus cloud contamination in sun photometer data. *Atmos. Environ.*, **45**, 6724-6731.
- Davis, G., 2007: History of the NOAA satellite program. *J. Appl. Remote Sens.*, **1**, 021504.
- Demaria, M., and J. Kaplan, 1994: Sea surface temperature and the maximum intensity of Atlantic tropical cyclones. *J. Climate*, **7**, 1324-1334.

Deschamps, P. Y., and T. Phulpin 1980: Atmospheric correction of infrared measurements of sea surface temperature using channels at 3.7, 11 and 12 Mm. *Bound.-Layer Meteor.*, **18**, 131-143.

Donlon, C., I. Robinson, K. S. Casey, J. Vázquez-Curvo, E. Armstrong, O. Arino, C. Gentemann, D. May, P. LeBorgne, J. Pioll, I. Barton, H. Beggs, D. J. S. Poulter, C. J. Merchant, A. Bingham, S. Heinz, A. Harris, G. Wick, B. Emery, P. Minnett, R. Evans, D. Llewellyn-Jones, C. Mutlow, R. W. Reynolds, H. Kawamura, and N. Rayner, 2007: The global ocean data assimilation experiment high-resolution sea surface temperature pilot project. *Bull. Amer. Meteorol. Soc.*, **88**, 1197-1213.

Fueglistaler, S., A. E. Dessler, T. J. Dunkerton, I. Folkins, Q. Fu, and P. W. Mote, 2009: Tropical tropopause layer. *Rev. Geophys.*, **47**, RG1004.

Gao, B.-C, Y. J. Kaufman, W. Han, and W. J. Wiscombe, 1998: Corection of thin cirrus path radiances in the 0.41.0 m spectral region using the sensitive 1.375 m cirrus detecting channel. *J. Geophys. Res.*, **103**, 32169-32176.

Garnier, A., J. Pelon, M. A. Vaughan, D. M. Winker, C. R. Trepte, and P. Dubuisson, 2015: Lidar multiple scattering factors inferred from CALIPSO lidar and IR retrievals of semi-transparent cirrus cloud optical depths over oceans. *Atmos. Meas. Tech.*, **8**, 2759-2774.

Harris, A., and E. Maturi, 2003: Assimilation of satellite sea surface temperature retrievals. *Bull. Amer. Meteor. Soc.*, **87**, 1575-1580.

Heymsfield, A., D. Winker, M. Avery, M. Vaughan, G. Diskin, M. Deng, V. Mitev, and R. Matthey, 2014: Relationships between ice water content and volume extinction coefficient from in situ observations for temperatures from 0° to 86°C: Implications for spacebornelidar retrievals. *J. Appl. Meteor. Climatol.*, **53**, 479-505.

Holz, R. E., S. A. Ackerman, F. W. Nagle, R. A. Frey, S. Dutcher, R. E. Kuehn, M. A. Vaughan, and B. A. Baum, 2008: Global Moderate Resolution Imaging Spectroradiometer (MODIS) cloud detection and height evaluation using CALIOP. *J. Geophys. Res.*, **113**, D00A19.

Hosoda, K., 2011: Algorithm for estimating sea surface temperatures based on Aqua/MODIS global ocean data. 2. Automated quality check process for eliminating cloud contamination. *J. Oceanogr.*, **67**, 791-805.

Huang, B., C. Liu, V. F. Banzon, H.-M. Zhang, T. R. Karl, J. H. Lawrimore, and R. S. Vose, 2016: Assessing the impact of satellite based observations in sea surface temperature trends. *Geophys. Res. Lett.*, **43**, 3431-3437.

Huang, J. F., N. C. Hsu, S. C. Tsay, M. J. Jeong, B. N. Holben, T. A. Berkoff, and E. J. Welton, 2011: Susceptibility of aerosol optical thickness retrievals to thin cirrus contamination during the BASE-ASIA campaign. *J. Geophys. Res.-Atmos.*, **116**, D08214.

Huang, J. F., N. C. Hsu, S. C. Tsay, Z. Y. Liu, M. J. Jeong, R. A. Hansell, J. Lee, 2013: Use of spaceborne lidar for the evaluation of thin cirrus contamination and screening in the Aqua MODIS Collection 5 aerosol products. *J. Geophys. Res.-Atmos.*, **118**, 6444-6453.

Jensen, E. J., O. B. Toon, H. B. Selkirk, J. D. Spinhirne, and M. R. Schoeberl, 1996: ON the formation and persistence of subvisible cirrus clouds near the tropical tropopause. *J. Geophys. Res.*, **101**, 21361-21375.

Kelley, J. G. W., D. W. Behringer, H. J. Thiebaut, and B. Balasubramanian, 2002: Assimilation of SST data into a real-time coastal ocean forecast system for the U.S. East Coast. *Wea. Forecasting*, **17**, 670-690.

Kilpatrick, K. A., G. P. Podestá, and R. Evans, 2001: Overview of the NOAA/NASA advanced very high resolution radiometer Pathfinder algorithm for sea surface temperature and associated matchup database. *J. Geophys. Res.*, **106**, 9179-9197.

Koner, P. K., A. Harris, and E. Maturi, 2015: A physical deterministic inverse method for operational satellite remote sensing: An application for sea surface temperature retrievals. *IEEE Trans. Geosci. Remote Sens.*, **53**, 5872-5888.

Le Borgne, P. Legendre, G., and Marsouin, A., 2007: Operational SST retrieval from METOP/AVHRR. *Proceedings of the Joint 2007 EUMETSAT Meteorological Satellite Conference and the 15th Satellite Meteorology & Oceanography Conference of the American Meteorological Society*. Amsterdam, The Netherlands. 24-28 September 2007.

Levanant, L., P. Marguinaud, L. Harang, J. Lelay, S. Pere, and S. Phillippe, 2007: Operational cloud masking for the O&SI SAF global METOP SST production. *Proceedings of the Joint 2007 EUMETSAT Meteorological Satellite Conference and the 15th Satellite Meteorology & Oceanography Conference of the American Meteorological Society*. Amsterdam, The Netherlands. 24-28 September 2007.

Li, X., W. Pichel, E. Maturi, P. Clemente-Coln, and J. Sapper, 2001: Deriving the operational nonlinear multichannel sea surface temperature algorithm coefficients for NOAA-15 AVHRR/3. *Int. J. Rem. Sens.*, **22**, 699-704.

Llewellyn-Jones, D. T., P. J. Minnett, R. W. Saunders, and A. M. Zavody, 1984: Satellite multichannel infrared measurements of sea surface temperature of the N.E. Atlantic Ocean using AVHRR/2. *Q. J. Roy. Meteorol. Soc.*, **110**, 613-631.

Mace, G. G., Q. Zhang, M. Vaughan, R. Marchand, G. Stephens, C. Trepte, and D. Winker, 2009: A description of hydrometeor layer occurrence statistics derived from the first year of merged Cloudsat and CALIPSO data. *J. Geophys. Res.*, **114**, D00A26.

McClain, E. P., W. G. Pichel, and C. C. Walton, 1985: Comparative performance of AVHRR-based multichannel sea surface temperatures. *J. Geophys. Res. Oceans*, **90**, 11587-11601.

Merchant, C. J., A. R. Harris, M. J. Murray, and A. M. Závody, 1999: Toward the elimination of bias in satellite retrievals of sea surface temperature: 1. Theory, modeling and interalgorithm comparison. *J. Geophys. Res.*, **104**, 23565-23578.

Merchant, C. J., and P. Le Borgne, 2004: Retrieval of sea surface temperature from space, based on modeling of infrared radiative transfer: Capabilities and limitations. *J. Atmos. Oceanic Technol.*, **21**, 1734-1746.

Merchant, C. J., P. Le Borgne, A. Marosuín, and H. Roquet, 2008: Optimal estimation of sea surface temperature from split-window observations. *Remote Sens. Environ.*, **112**, 2469-2484.

Merchant, C. J., A. R. Harris, E. Maturi, O. Embury, S. N. MacCallum, J. Mittaz, and C. P. Old, 2009: Sea Surface Temperature Estimation from the Geostationary Operational Environmental Satellite-12 (GOES-12). *J. Atmos. Oceanic Technol.*, **26**, 570-581.

Merchant C. J., O. Embury, N.A. Rayner, D. I. Berry, G. Corlett, K. Lean, K. L. Veal, E. C. Kent, D. Llewellyn-Jones, J. J. Remedios, and R. Saunders, 2012: A twenty-year independent record of sea surface temperature for climate from Along Track Scanning Radiometers. *J. Geophys. Res.*, **117**, C12013.

Miller, B. I., 1958: On the maximum intensity of hurricanes. *J. Meteor.*, **15**, 184-195.

Minnett, P. J., R. H. Evans, K. R. Turpie, G. Podestá, K. Kilpatrick, G. Szczodrak, M. A. Izaguirre, E. Williams, S. Walsh, W. Baringer, A. Chambers and R. M. Reynolds, 2013: Assessment of Suomi-NPP VIIRS sea surface temperature retrievals. *University of Miami*.

Miyazawa, Y., H. Murakami, T. Miyama, S. M. Varlamov, X. Guo, T. Waseda, and S. Sil, 2013: Data assimilation of the high-resolution sea surface temperature obtained from the Aqua-Terra satellites (MODIS-SST) using an ensemble Kalman filter. *Remote Sens.*, **5**, 3123-3139.

Petrenko, B., A. Ignatov, Y. Kihai, J. Stroup, and P. Dash, 2014: Evaluation and selection of SST regression algorithms for JPSS VIIRS. *J. Geophys. Res.*, **119**, 4580-4599.

Reynolds, R. W., and T. M. Smith, 1994: Improved global sea surface temperature analyses using optimum interpolation. *J. Climate*, **7**, 929-948.

Ricchiazzi, P., S. Yang, C. Gautier, and D. Sowle, 1998: SBDART: A research and teaching software tool for plane-parallel radiative transfer in the earth's atmosphere. *Bull. Amer. Meteorol. Soc.*, **79**, 2101-2114.

Roemmich, D, G. C. Johnson, S. Riser, R. Davis, J. Gilson, W. B. Owens, S. L. Garzoli, C. Schmid, and M. Ignaszewski, 2009: The Argo program: Observing the global ocean with profiling floats. *Oceanogr.*, **22**, 34-43.

Sassen, K, and B. S. Cho, 1992: Subvisual-thin cirrus lidar dataset for satellite verification and climatological research. *J. Appl. Meteorol.*, **31**, 1275-1285.

Sassen, K, Z. Wang, and D. Liu, 2008: Global distribution of cirrus clouds from CloudSat/Cloud Aerosol Lidar and Infrared Pathfinder Satellite Observations (CALIPSO) measurements. *J. Geophys. Res.*, **113**, D00A12.

Stephens, G. L., D. G. Vane, R. J. Boain, G. G. Mace, K. Sassen, Z. Wang, A. J. Illingworth, E. J. O'Connor, W. B. Rossow, S. L. Durden, S. D. Miller, R. T. Austin, A. Benedetti, C. Mitrescu, and the CloudSat Science Team, 2002: The CloudSat mission and the A-Train: A new dimension of space-based observations of clouds and precipitation. *Bull. Amer. Meteorol. Soc.*, **83**, 1771-1790.

Tang, Y., R. Kleeman, and A. M. Moore, 2004: SST assimilation experiments in a tropical Pacific Ocean model. *J. Phys. Oceanogr.*, **34**, 623-642.

Toth, T. D., J. Zhang, J. R. Campbell, J. S. Reid, Y. Shi, R. S. Johnson, A. Smirnov, M. A. Vaughan, and D. M. Winker, 2013: Investigating enhanced Aqua MODIS aerosol optical depth retrievals over the mid-to-high latitude Southern Oceans through intercomparison with co-located CALIOP, MAN, and AERONET data sets. *J. Geophys. Res. Atmos.*, **118**, 4700-4714.

Vaughan, M. A., K. A. Powell, R. E. Kuehn, S. A. Young, D. M. Winker, C. A. Hostetler, W. H. Hunt, Z. Liu, M. J. McGill, and B. J. Getzewich, 2009: Fully automated detection of cloud and aerosol layers in the CALIPSO lidar measurements. *J. Atmos. Oceanic. Technol.*, **26**, 2034-2050.

Vázquez-Cuervo, J., and E. Armstrong, 2004: The effect of aerosols and clouds on the retrieval of infrared sea surface temperatures. *J. Climate*, **11**, 3921-3933.

Virts, K. S., 2009: Cirrus in the tropical tropopause transition layer: Formation mechanisms and influence of the local and planetary-scale environment. M.S. thesis, Dept. of Atmospheric Sciences, University of Washington, 108 pp.

Walton, C. C., 1988: Nonlinear multichannel algorithms for estimating sea surface temperature with AVHRR satellite data. *J. Appl. Meteor.*, **27**, 115-124.

Walton, C. C., W. G. Pichel, J. F. Sapper, and D. A. May, 1998: The development and operational application of nonlinear algorithms for the measurement of sea surface temperatures with the NOAA polar-orbiting environmental satellites. *J. Geophys. Res.*, **103**, 27999-28012.

Winker, D. M., Vaughan, M. A., Omar, A., Hu, Y., Powell, K.A., Liu, Z., Hunt, W. H., and Young, S. A., 2009: Overview of the CALIPSO Mission and CALIOP Data Processing Algorithms. *J. Atmos. Ocean. Tech.*, **26**, 2310-2323.

Winker, D. M., J. Pelon, J. A. Coakley Jr., S. A. Ackerman, R. J. Charlson, P. R. Colarco, P. Flamant, Q. Fu, R. M. Hoff, C. Kittaka, T. L. Kubar, H. Le Treut, M. P. McCormick, G. Megie, L. Poole, K. Powell, C. Trepte, M. A. Vaughan, and B. A. Wielicki, 2010: The CALIPSO mission: A Global 3D view of aerosols and clouds. *Bull. Amer. Meteorol. Soc.*, **91**, 1211-1229.

Wu, X., W. P. Menzel, and G. S. Wade, 1999: Estimation of sea surface temperatures using GOES-8/9 radiance measurements. *Bull. Amer. Meteor. Soc.*, **80**, 1127-1138.

Yang, P., H. Wei, H. Huang, B. A. Baum, Y. X. Hu, G. W. Kattawar, M. I. Mishchenko, and Q. Fu, 2005: Scattering and absorption property database for nonspherical ice particles in the near- through far-infrared spectral region. *Appl. Opt.*, **44:26**, 5512-5523.

Young S. A., and M. A. Vaughan, 2009: The retrieval of profiles of particulate extinction from Cloud-Aerosol Lidar Infrared Pathfinder Satellite Observations (CALIPSO) data: Algorithm description. *J. Atmos. Oceanic. Technol.*, **26**, 1105-1119.